AGU PUBLICATIONS

JGR

Journal of Geophysical Research: Earth Surface

RESEARCH ARTICLE

10.1002/2014JF003252

The life of a meander bend: Connecting shape and dynamics via analysis of a numerical model

Jon Schwenk[1], Stefano Lanzoni[2], and Efi Foufoula-Georgiou[1]

[1]Department of Civil, Environmental, and Geo- Engineering, Saint Anthony Falls Laboratory, University of Minnesota, Minneapolis, Minnesota, USA, [2]Dipartimento di Ingegneria Idraulica, Marittima Ambientale e Geotecnica, Università di Padova, Padua, Italy

Key Points:
- Automatic extraction of individual meanders from long-term numerical models
- Three dynamic metrics show how single bends grow and respond to perturbations
- Cutoff meander geometry contains the signature of its formative dynamics

Supporting Information:
- Readme
- Codes S1

Correspondence to:
J. Schwenk,
jonschwenk@gmail.com

Citation:
Schwenk, J., S. Lanzoni, and E. Foufoula-Georgiou (2015), The life of a meander bend: Connecting shape and dynamics via analysis of a numerical model, *J. Geophys. Res. Earth Surf.*, *120*, 690–710, doi:10.1002/2014JF003252.

Received 18 JUN 2014
Accepted 19 FEB 2015
Accepted article online 23 FEB 2015
Published online 10 APR 2015

Abstract Analysis of bend-scale meandering river dynamics is a problem of theoretical and practical interest. This work introduces a method for extracting and analyzing the history of individual meander bends from inception until cutoff (called "atoms") by tracking backward through time the set of two cutoff nodes in numerical meander migration models. Application of this method to a simplified yet physically based model provides access to previously unavailable bend-scale meander dynamics over long times and at high temporal resolutions. We find that before cutoffs, the intrinsic model dynamics invariably simulate a prototypical cutoff atom shape we dub *simple*. Once perturbations from cutoffs occur, two other archetypal cutoff planform shapes emerge called *long* and *round* that are distinguished by a stretching along their long and perpendicular axes, respectively. Three measures of meander migration—growth rate, average migration rate, and centroid migration rate—are introduced to capture the dynamic lives of individual bends and reveal that similar cutoff atom geometries share similar dynamic histories. Specifically, through the lens of the three shape types, *simples* are seen to have the highest growth and average migration rates, followed by *rounds*, and finally *longs*. Using the maximum average migration rate as a metric describing an atom's dynamic past, we show a strong connection between it and two metrics of cutoff geometry. This result suggests both that early formative dynamics may be inferred from static cutoff planforms and that there exists a critical period early in a meander bend's life when its dynamic trajectory is most sensitive to cutoff perturbations. An example of how these results could be applied to Mississippi River oxbow lakes with unknown historic dynamics is shown. The results characterize the underlying model and provide a framework for comparisons against more complex models and observed dynamics.

1. Introduction

Meandering rivers have intrigued researchers for decades with their beautiful esthetics, complex dynamics, and extraordinary cutoffs. The first physically based theory answering the question of why rivers meander was not introduced until the early 1980s [*Ikeda et al.*, 1981] despite decades of study on the problem (see *Seminara* [2006] for a thorough review). Meandering channels seem to be universal; besides the ubiquitous terrestrial meandering rivers, they are also found in submarine [*Imran et al.*, 1999; *Lazarus and Constantine*, 2013] and other planetary [*Weihaupt*, 1974; *Irwin et al.*, 2005; *Lorenz et al.*, 2008; *Ori et al.*, 2013] environments. Understanding meandering river dynamics is important for a host of engineering and geologic applications including stream restoration [*Kondolf*, 2006], bridge design [*Lagasse et al.*, 2004], agriculture management [*Graf*, 2008], stratigraphic interpretation [*van de Lageweg et al.*, 2013], oil discovery [*Henriquez et al.*, 1990; *Swanson*, 1993], and even predator-prey population dynamics [*Beschta and Ripple*, 2012].

A concerted effort emerged in the 1960s from within the geomorphology community to measure meander planform changes [*Hooke*, 1977] and to explain mechanisms driving observed planform evolution [*Leopold and Wolman*, 1960]. This work rested upon previous research that developed metrics of planform geometry through analysis of both real [*Jefferson*, 1902; *Dury*, 1955; *Leopold and Wolman*, 1957] and experimental [*Quraishy*, 1944; *Friedkin*, 1945] meanders. Since then, significant contributions have been made via an abundance of field studies that apply these metrics to real river centerlines derived from combinations of historic maps [*Hooke and Redmond*, 1989], aerial photography [*Yao et al.*, 2012; *Nagata et al.*, 2014], and field surveys [*Legleiter*, 2014].

Despite these studies' significant contributions toward deciphering meandering river dynamics, the difficulty of acquiring long-time, high temporal and spatial resolution channel migration data has hampered

efforts to fully quantify dynamics from observations alone [*Hooke*, 2003; *Hooke and Yorke*, 2010]. Numerical modeling has thus become a primary tool for understanding meandering complexity and emergent behavior. Long-term meander models simulate migrating channels over centuries to millennia, providing insight into otherwise inaccessible dynamics. These models are useful for both practical [e.g., *Xu et al.*, 2011; *Jackson and Austin*, 2013] and theoretical investigations. Theoretical analyses of such simulations typically focus on either reach-scale measures such as sinuosity [*Crosato*, 2009; *Frascati and Lanzoni*, 2009], mean meander wavelength [*Camporeale et al.*, 2005], or mean curvature [*Howard and Hemberger*, 1991]. However, to the best of our knowledge no study has considered either observed or modeled well-resolved temporal dynamics of individual meander bend evolutions. Here we present a new tool for identifying and extracting the lives of these individual meander bends, dubbed "atoms" and defined extensively in section 3, from the centerline output of long-time channel migration models. Our method makes accessible the lifespan of individual meander bends from inception until cutoff by tracking the two end indices of a set of cutoff nodes backward through time.

Our choice to focus primarily on bend-scale morphodynamics is guided by its emergence as perhaps the only natural intermediate scale between the cross-section and river-valley scales. Meandering river relicts are frequently preserved at bend scales through the formation of oxbow lakes or scroll bars. Engineering designs are often concerned only with morphodynamics of a single bend [e.g., *Shields et al.*, 2005; *Rossell and Ting*, 2013]. Besides the pragmatism of the bend scale, physically based meander migration theories [*Ikeda et al.*, 1981; *Zolezzi and Seminara*, 2001] predict a nonlocal memory effect on local hydrodynamics from nearby curvatures that becomes approximately negligible beyond a single meander wavelength. In addition to being a natural scale for analysis of meandering rivers, the bend-scale approach promises at least three advantages toward understanding river meandering dynamics.

First, a bend-scale framework may help reinterpret previous work on meander loop classification by linking static planform shapes to historic dynamic signatures. Classification schemes for oxbow lakes [*Weihaupt*, 1974] and river meanders [*Leighly*, 1936; *Melton*, 1936] are well developed, but as *Schumm* [1985] points out, the goal of such classifications is to connect form and process. Although modes of planform migration have been well established [*Hooke*, 1984; *Lagasse et al.*, 2003], linking these modes to underlying physical processes has largely remained an open research area: which dynamic behaviors are correlated with which planform shapes? Conversely, inferring dynamics from static planform shapes can be useful for paleochannel studies [*Baker et al.*, 1987].

Second, meander bends provide a more refined basis to compare model outputs to both real rivers and other models by avoiding reach-wide-averaged metrics. *Camporeale et al.* [2005] found three contemporary models of increasing complexity to be statistically indistinguishable in their spatially averaged meander wavelengths and curvatures. The dynamic details resulting from the different physics and assumptions of each model are smoothed over by such reach-wide averaging. Bend-scale measures that dissect reach-wide ones are better suited for describing and explaining differences in model outputs because they provide full distributions rather than sole averages. The problem of statistical averaging in meandering river studies has been known for awhile [*Hooke*, 1984] but remains largely unaddressed because tools have not yet been developed. Meander loops are already inherently difficult to classify with single measures [*Ferguson*, 1975], so averaging over already averaged quantities results in substantial information loss. An attempt to overcome these difficulties was put forward by *Howard and Hemberger* [1991] who proposed a suite of 40 morphometric variables to distinguish between modeled and natural planforms. However, their work focused only on spatial analyses of these variables rather than their dynamics. By combining spatial and temporal analyses, our method can both effectively diagnose a model's dynamic accuracy and elucidate how accounting for different physical processes affects channel migration dynamics.

Third, a recent special issue on meandering [*Güneralp et al.*, 2012] highlights the apparent gap between holistic and reductionist philosophies of river meandering. In the format of an entertaining philosophical dialog, *Seminara and Pittaluga* [2012] discuss the incongruities of holistic analyses performed using reductionist-based migration models. For example, researchers have tested meandering rivers for nonlinear dynamics [*Montgomery*, 1993; *Perucca et al.*, 2005], chaotic dynamics [*Frascati and Lanzoni*, 2010], self-similarity [*Leopold and Wolman*, 1960; *Stolum*, 1998], self-organized criticality [*Stolum*, 1996], and fractality [*Snow*, 1989; *Montgomery*, 1996], all concepts that imply the presence of energy at many space-time scales.

Accessible bend-scale dynamics will help link local physical processes with reach-scale phenomena by providing a coherent intermediate scale between global and local.

The focus of this paper is primarily on the first of these three issues, i.e., connecting simulated meander geometries with their formative dynamics, but we hope the utility of our study toward refined model comparisons and bridging scales of analysis becomes clear from the work herein. This paper is structured as follows: section 2 describes the numerical migration model we used, section 3 explains how individual bends are extracted through time, section 4 presents some results and insights of the analysis followed by discussion in section 5. Section 6 concludes with general remarks and future work.

2. Model Description

Long-time meander migration models usually have four distinct components: (1) a morphodynamic model relating the flow field to bank migration; (2) a hydrodynamic model relating the channel geometry (i.e., curvature and cross-sectional geometry) to the flow field; (3) an evolution equation relating bank migration to planform geometry; and (4) a model accounting for cutoff events [e.g., *Frascati and Lanzoni*, 2009]. The third and fourth components render numerical models necessary to account for the strong nonlinearities associated with the kinematics of channel planform evolution and abrupt channel shortening due to cutoff processes [*Camporeale et al.*, 2008]. By adopting simple first and second components (i.e., morphodynamic and hydrodynamic models) here, our resulting dynamics provide insight into the geometric nonlinear interactions that are present in all models of long-time channel migration.

2.1. Morphodynamic and Hydrodynamic Model

Several models are currently available to treat bank erosion [*Hasegawa*, 1977; *Parker et al.*, 2011; *Motta et al.*, 2012a] and to describe the flow field in meandering channels with arbitrary distribution of the channel axis curvature [*Ikeda et al.*, 1981; *Zolezzi and Seminara*, 2001; *Bolla Pittaluga et al.*, 2009] and channel width [*Frascati and Lanzoni*, 2013; *Eke et al.*, 2014]. In the following, however, we prefer to keep the hydrodynamic and morphodynamic models at the lowest level of refinement. In fact, our aim is to develop a new methodology for characterizing individual bend dynamics that can be used independently of the degree of approximation and physical realism embodied by the adopted morphodynamic and hydrodynamic models. We thus follow the work of *Hasegawa* [1977] and *Ikeda et al.* [1981] who first introduced a dynamic approach for bank erosion and a linearized flow field model in sinuous channels, providing a relatively simple framework for computational modeling (hereafter called HIPS after its authors). A suite of models has emerged following their pioneering work that share the following morphodynamic model:

$$\zeta = E_o U_b \tag{1}$$

in which the lateral migration rate, ζ, at a point along a channel centerline is the product of a bank erodibility coefficient E_o and an excess bank velocity U_b resulting from perturbations in channel curvature and bar formation. This linear relationship for migration has been validated by the field campaigns of *Hasegawa* [1977], *Odgaard* [1987], and *Pizzuto and Meckelnburg* [1989]. The erodibility coefficient E_o is generally considered representative of the geotechnical bank properties [*Wallick et al.*, 2006] whose functional dependencies remain unknown but include near-bank vegetation, failure mechanism, and local channel geometry effects among others [*Constantine et al.*, 2009a]. In predictive models E_o is typically calibrated using past channel configurations [e.g., *Mosselman*, 1998; *Larsen and Anderson*, 2002; *Micheli and Kirchner*, 2002], although studies have also investigated its effects on migration dynamics [*Sun and Meakin*, 1996; *Perucca et al.*, 2007; *Constantine et al.*, 2009a; *Güneralp and Rhoads*, 2011].

The hydrodynamic model for U_b is developed by casting the Saint Venant shallow water equations in an intrinsic coordinate system, where the $s = S/B$ coordinate refers to the dimensionless streamwise direction, $n = N/B$ coordinate to the transverse direction, and B is the channel half width (Figure 1). Lowercase variables are dimensionless and variables subscripted with $_o$ denote channel-averaged values. Scaling the channel axis curvature as $c = CR_o$, where R_o is the minimum value of the radius of curvature within the investigated reach, reveals the existence of the usually small parameter $\nu_o = B/R_o$. The relevant variables can then be expanded in terms of ν_o, and a linear perturbation analysis gives the following linear solution for excess flow velocity at the bank under assumptions of constant channel width and spatially constant friction factor:

$$u_b(s) = \left[u_b(s=0) + \nu_o c(s=0)\right] e^{\lambda_o s} - \nu_o \left[c(s) + \frac{\lambda_o}{2}(F_o^2 + A)\int_0^s c(\xi) e^{\lambda_o (s-\xi)} \mathrm{d}\xi\right] \tag{2}$$

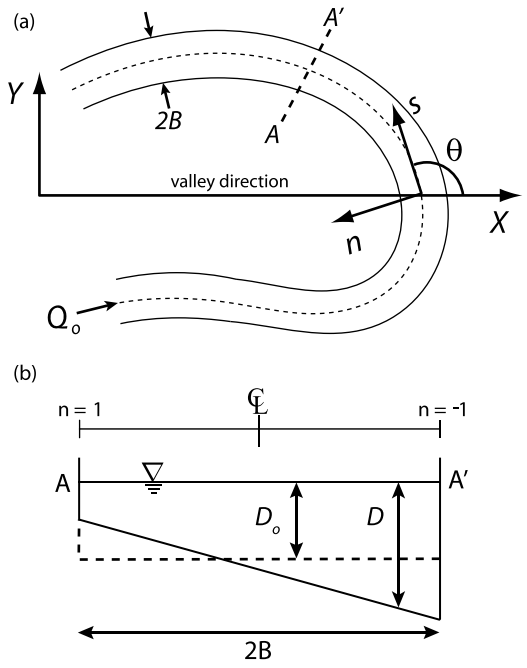

Figure 1. Coordinate systems and modeling variables. (a) Planform view of a meander of constant width 2*B*. The *s* coordinate always points in the streamwise direction, and the *X* axis is aligned with the valley direction. (b) Cross section of the channel. The outer bank corresponds to $n=1$ and at the centerline $n=0$.

where the dimensionless excess bank velocity $u_b = U_b/U_o$ and channel axis curvature $c = CR_o$ are $\mathcal{O}(1)$ quantities, $\lambda_o = -2\beta C_{fo}$ is a characteristic exponent where $\beta = B/D_o$, C_{fo} is the spatially constant friction factor, $F_o^2 = U_o^2/gD_o$, and A is a constant slope factor expressed as $\alpha + 1$ after [*Johannesson and Parker*, 1985] where α is a dimensionless parameter related to the across-stream bed slope. Our simulation parameters, based on bankfull flow conditions of the Beatton River in Canada originally reported by *Parker and Andrews* [1986], are as follows: $B = 35$ m, $Q_o = 325.6$ cm, $C_{f,o} = 0.0036$, $E_o = 1.85 \times 10^{-8}$, $\alpha = 10$, and $s_v = 0.0067$. The upstream boundary condition on u_b was set to zero, prohibiting migration of the first node, and boundary conditions on curvature are discussed in section 2.2.2. The convolution integral in equation (2) implies that the excess bank velocity at a given section is affected not only by the local value of the axis curvature but also by the hydrodynamics and morphodynamics of the upstream reaches. In particular, influence is exerted only in the downstream direction. This is a direct consequence of the decoupled treatment of sediment-flow dynamics (i.e., prescribed transverse bed slope) that precludes the model's accounting for overdeepening [*Struiksma et al.*, 1985], resonance [*Blondeaux and Seminara*, 1985], and upstream influence [*Lanzoni and Seminara*, 2006]. The hydrodynamic model does not explicitly account for secondary flow momentum convection and instead uses the surrogate parameter A [*Johannesson and Parker*, 1989].

We should note that many of the assumptions and simplifications of the original HIPS work have since been relaxed, including small-curvature restrictions [*Blanckaert and de Vriend*, 2010], constant width [*Luchi et al.*, 2011; *Frascati and Lanzoni*, 2013], prescribed width [*Eke et al.*, 2014], constant discharge [*Hall*, 2004; *Asahi et al.*, 2013], deformable bed [*Johannesson and Parker*, 1989; *Zolezzi and Seminara*, 2001], two dimensionality [*Rüther and Olsen*, 2007], linearity [*Bolla Pittaluga et al.*, 2009], and single-threadedness [*Coulthard and Wiel*, 2006]. *Camporeale et al.* [2007] reviews two decades' progress in meander migration modeling, while *Parker et al.* [2011] offers a recent critical assessment of the HIPS formulation. Despite their significant simplifications, HIPS models can produce reach-scale planforms and dynamics that under subresonant conditions are statistically similar to real planforms with regards to fractal dimension of river lengths [*Stolum*, 1996], size-frequency distributions of oxbow lakes [*Stolum*, 1998], and planimetric form [*Frascati and Lanzoni*, 2009]. Additionally, *Camporeale et al.* [2005] compared a HIPS model with two more sophisticated models [*Johannesson and Parker*, 1989; *Zolezzi and Seminara*, 2001] and found that the average river wavelength and curvature approached a statistically steady state independent of model complexity. Under subresonant conditions the HIPS model we employ here sufficiently captures the first-order, curvature-forced processes driving river meandering over long times and hence is suitable for developing new tools that characterize the individual bend dynamics.

2.2. Numerical Environment

The basic steps of our meander migration model proceed as follows: (1) input a centerline and reach-wide hydraulic variables, (2) solve hydrodynamics throughout the reach, (3) migrate the channel, (4) locate and perform cutoffs, (5) check node spacing criteria, and (6) update reach-averaged variables. The model was implemented in MATLAB and takes advantage of parallel processing for solving the hydrodynamics and locating and performing cutoffs. Source code for the model and extraction algorithm is provided in the supporting information.

2.2.1. Gridding and Numerical Migration

Our numerical model uses both Cartesian and intrinsic coordinates, as shown in Figure 1. The channel centerline is first discretized into a series of initially evenly spaced nodes every $B/2$. Constant channel width and prescribed bed topography permit reconstruction of the channel geometry from its centerline so no other planform variables are saved. Following *Sun and Meakin* [1996], the initial planform configuration is a straight line parallel to the valley axis with small random Gaussian perturbations $\sim \mathcal{N}(0, 0.01B)$ in the streamwise-perpendicular direction. At every time step, each centerline node migrates according to equation (1) and

$$\frac{dX_i}{dt} = -\zeta_i \sin\theta_i \tag{3}$$

$$\frac{dY_i}{dt} = \zeta_i \cos\theta_i \tag{4}$$

for node i, where θ_i is the ith angle between the downstream channel direction and the x axis. As the nodes of the channel centerline migrate, spacing between nodes may become either too large or too small. If the distance between nodes becomes too large, numerical accuracy suffers and the model tends toward instability. Conversely, very small node spacings can introduce errors associated with the computation of curvature. *Crosato* [2007] suggests based on empirical analysis that optimal node spacing is on the order of $2B$; we adopted a maximum node spacing threshold value of $\frac{4}{3}B$. Where this threshold was exceeded, a parametric cubic spline [*Duris*, 1977; *de Boor*, 2001] fit to the preceding and following three points (six nodes total) determined the coordinates of the interpolated node. In rare cases, especially after cutoff, node spacing could become too small so a lower threshold of $\frac{B}{5}$ was maintained. The time step $\triangle t = 0.2$ years was chosen small enough to ensure numerical accuracy and stable computations [*Crosato*, 1990; *Sun and Meakin*, 1996; *Lanzoni and Seminara*, 2006].

2.2.2. Computation of Curvature

The hydrodynamic model is primarily driven by variations in curvature along the centerline, yet methods of digital curvature estimation from discrete nodes are often inaccurate and biased [*Worring and Smeulders*, 1993]. Evidence suggests that long-time meander migration models are sensitive to small perturbations [see *Sun and Meakin*, 1996, Figure 4], so even small inaccuracies in curvature estimation could significantly alter the simulated planform. One of three mathematically equivalent definitions of curvature κ is usually employed in meander migration models, but their accuracies are dependent on both gridding and computation method. For a planar curve in Cartesian coordinates, $\kappa_1 = \frac{|x'y'' - y'x''|}{(x'^2+y'^2)^{3/2}}$, where the prime denotes a derivative taken with respect to the S direction. If derivatives are approximated via a first-order differencing scheme, the denominator equals unity leading to the form in *Johannesson and Parker* [1985, equation (28)]. A second widely used method exploits the definition $\kappa_2 = d\theta/dS$, where first-order differencing gives $\theta_i = \arctan\left(\frac{y_{i+1}-y_i}{x_{i+1}-x_i}\right)$. The third method and one we employ considers $\kappa_3 = 1/R$, where the radius of curvature

$$R = \frac{\sqrt{(\mathbf{a_x^2} + \mathbf{a_y^2})(\mathbf{b_x^2} + \mathbf{b_y^2})(\mathbf{c_x^2} + \mathbf{c_y^2})}}{2\left(\mathbf{a_y b_x} - \mathbf{a_x b_y}\right)} \tag{5}$$

for $\mathbf{a_x} = x_i - x_{i-1}$, $\mathbf{b_x} = x_{i+1} - x_{i-1}$, $\mathbf{c_x} = x_{i+1} - x_i$. This formula for R arises from geometric considerations showing that the radius of a circle defined by three points is the area of their triangle divided by the product of the lengths of their sides; it provided the stablest and smoothest curvature signal among the three methods (Figure 2), preventing the need for a smoothing filter as often required by numerical meander migration models [*Crosato*, 2007]. Our selected method for curvature computation may not produce similar results in other numerical environments because the computation of curvature depends also on grid resolution and configuration, derivative estimation method, and computational precision.

An upstream boundary condition on curvature must be applied at each time step; we used a periodic boundary condition of $c(s=0)_t = c(s=\text{end}-1)_{t-1}$, where end refers to the final node along the centerline and $_t$ denotes the model's current time step. The downstreammost curvature value $c(s=\text{end})$ requires a linearly interpolated centerline node downstream of the reach at each time step; information only travels downstream in models that do not account for resonance [*Lanzoni and Seminara*, 2006], so any errors introduced by this interpolation will not propagate upstream into the domain.

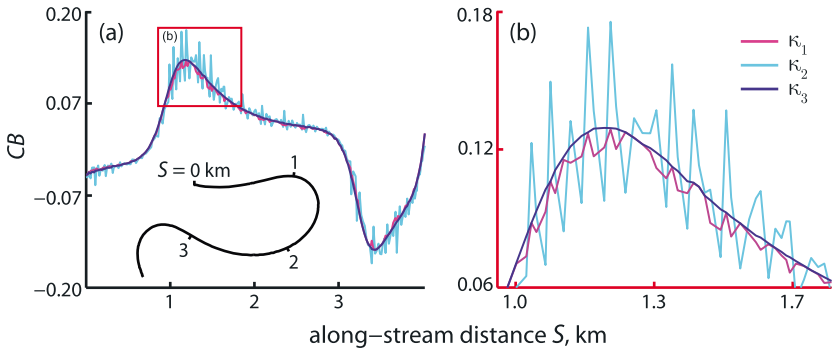

Figure 2. (a) Comparison of three different curvature computation methods for the bend. The 4 km bend is scaled such that the aspect ratio is 1:1, and the upstream end is denoted by $S=0$. (b) The box around the region of maximum curvature in Figure 2a is expanded. Definitions for computing each κ_i are discussed in section 2.2.2. Derivatives are estimated by first-order differencing. We employ κ_3 for the analyses herein.

2.2.3. Cutoffs

Natural meandering rivers typically cut off via either chute or neck mechanisms [*Allen*, 1965]. Neck cutoffs occur when migrating river reaches intersect themselves, while chute cutoffs "short circuit" neck cutoffs with a connecting channel usually during flood flows. Chute cutoffs have been well-documented [e.g., *Lewis and Lewin*, 1983; *Gay et al.*, 1998], but the various mechanisms driving their occurrence remain relatively unexplored and therefore difficult to predict [*Seminara*, 2006; *Constantine et al.*, 2009b]. *Howard* [1996] presents a meander migration model that takes a stochastic approach to chute cutoffs. Because of the poor predictability of chute cutoffs, our model accounts only for neck cutoffs.

Neck cutoffs are identified when two nodes of stream centerline are separated by a distance less than or equal to $2B$. This search begins at the upstream-most centerline node and works downstream, removing cutoffs along the way. The built-in MATLAB function *rangesearch* builds a *k*-d tree to reduce search time of closest nodes from $\mathcal{O}\left(m^2\right)$ time complexity to $\mathcal{O}\left(\log(m)\right)$, where m is the number of centerline nodes. If intersections are detected, the portion of centerline between the intersecting segments is removed, a single node is added across the cutoff via cubic spline interpolation, and a local Savitztky-Golay filter [*Orfanidis*, 1996] is applied to smooth the resulting discontinuity. *Camporeale et al.* [2005] offer an algorithm for cutoff search that operates in apparently $\mathcal{O}(m)$ time.

3. Atom Tracking Method

In this work we seek to explore the dynamics of simulated individual meanders from their inception until cutoff, requiring a robust and accurate method for continuously identifying meander loops. A meander loop is typically defined as the reach of stream between two points of zero curvature known as inflection points. For a continuous function, curvature can be computed analytically as the second derivative and the inflection points easily obtained, but for discrete nodes inflection point detection becomes more complicated. In general, inflection points are not located exactly at grid nodes, so they must be somehow interpolated between two nodes of oppositely-signed curvature. The simplest identification method assigns the inflection point to the node with the smaller absolute curvature value. However, as discussed in section 2.2.2, discrete curvature computations can cause complications connected with curvature calculation method which might lead to misidentifying the inflection node [*Worring and Smeulders*, 1993; *Utcke*, 2003]. Additionally, spurious flexes especially along nearly straight sections of the curve will identify more than two inflection points per meander bend [e.g., *Güneralp and Rhoads*, 2007, Figure 9], rendering ambiguous meander endpoints. These flexes preclude robust algorithms from properly detecting inflection points smoothly through time and therefore require ad hoc rules. For example, *Howard and Hemberger* [1991] proposed identifying nodes as inflection points when

$$\text{sign}\left(C_i + C_{i-1}\right) \neq \text{sign}\left(C_{i+1} + C_{i+2}\right) \tag{6}$$

where C_i is the curvature of the node in question. Others such as *Carson and Lapointe* [1983] have used minimum length and minimum curvature criteria.

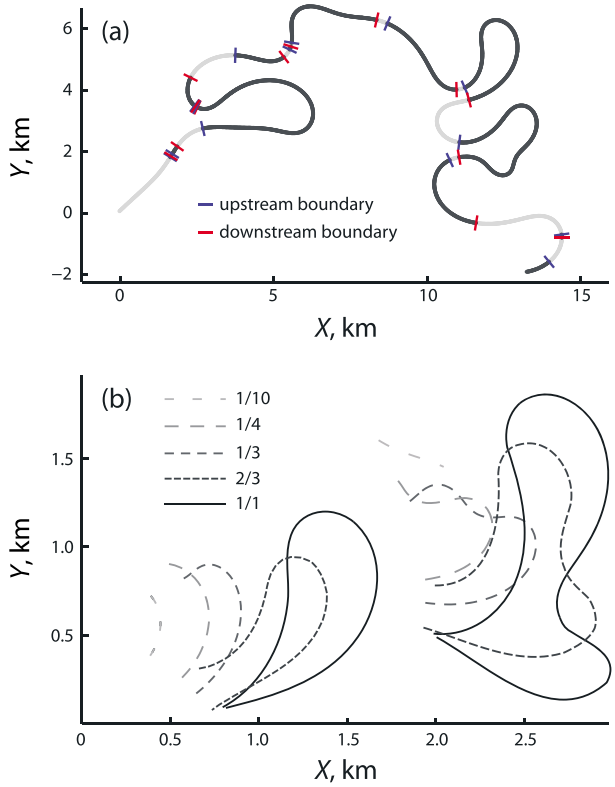

Figure 3. (a) The dissection of a centerline reach into atoms. The dark portions of centerline are atoms whose extents are marked by blue (upstream) and red (downstream) boundaries. Some atoms are as short as three nodes, while some are approaching cutoff. The lighter portions of the centerline are fractions of atoms whose boundaries are yet unknown because their cutoff nodes do not yet exist. (b) The development of two atoms' centerlines from inception until cutoff. Legend values represent the fraction of atom length L_a to its length at cutoff L_{cut}, i.e., 1/10 shows an atom at one-tenth its cutoff length (near inception) and 1/1 shows the atom at cutoff. The left atom shows the growth of an unperturbed single loop, while the right atom develops a second loop due to a cutoff immediately upstream that occurs between 1/4 and 1/3. This figure highlights the ambiguity of atom inception; as tracking proceeds backward, the atom loses its loop-like form and becomes a segment of almost constant-curvature centerline.

For spatial analyses of meanders [e.g., *Howard and Hemberger*, 1991; *Camporeale et al.*, 2005; *Güneralp and Rhoads*, 2010], simple meander loop detection methods based on inflection points are usually sufficient because small errors in the inflection point location only slightly affect average meander measures of wavelength, amplitude, or skewness. For estimating such properties dynamically (as they change through time), however, errors in detection can lead to substantial inaccuracies in the time series. Therefore, dynamic investigations require a robust and continuous detection of meander endpoints for any given planform.

We found ad hoc methods to be unreliable when applied to the various evolving complex shapes produced by the model, so a new method was developed. With only a few modifications, this method can be applied to any model that tracks a set of centerline nodes through time. Instead of defining meander bends as reaches of stream between inflection points, we take another approach and introduce *atoms*. An atom is simply a river reach that evolves in time and eventually intersects itself to become a cutoff meander loop (Figure 3).

Our method for identifying an atom continuously through time requires that its cutoff locations (or indices) be known a priori. The indices of the first and last nodes of the known cutoff may then be tracked by moving backward through time, adjusting the cutoff indices as nodes were added or removed upstream. Figure 3b shows two atoms developing from apparent squiggles of centerline into full meander loops. A single-loop atom usually has an upstream and downstream tail defined as the length of stream between the cutoff node and the inflection node (see Figure 9 and discussion in section 4.2), while its head corresponds to the traditional definition of a meander bend as the length of stream between inflection points containing the apex of the loop. We should note that although the definition of an atom does not preclude its application to real rivers, the condition that the cutoff location be known beforehand limits its applicability. In the following section we present an unambiguous method for identifying atoms from simulated meander migration models.

3.1. Numerical Implementation

An atom's endpoints are tracked backward through time with a node accounting algorithm beginning with the positions of the first and last indices of a set of cutoff nodes, or the two *cutoff indices*. This algorithm, while conceptually simple, can be tricky to implement. It requires that the model saves at each time step (i) the channel centerline and (ii) the time and locations of any added or removed nodes including the time

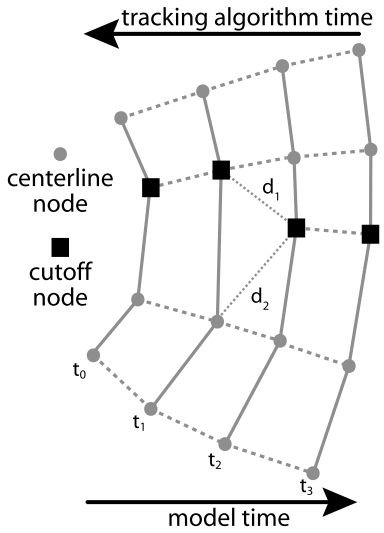

Figure 4. How the tracking algorithm deals with centerline node interpolations. Circles are centerline nodes and squares are the cutoff node being tracked by the algorithm. As the model advances in time, the distance between nodes increases until it becomes larger than the node spacing threshold, at which time a new node is interpolated at t_2. Conversely, the algorithm that tracks the cutoff node works backward through time and sees the cutoff node removed after t_2. The cutoff node at t_1 is selected based on the shortest distance to the nearest neighboring nodes; in this case $d_1 < d_2$.

and locations of cutoffs. The algorithm then marches backward in time, adjusting the two cutoff indices to account for nodes inserted due to spacing threshold requirements and/or removed due to cutoffs, smoothing or grid spacing.

The heart of the meander bend tracking algorithm is an accounting scheme which simply adds or subtracts to the original cutoff indices in the reverse order that nodes were added or removed, respectively. For example, a typical meander migration model implementation might progress as follows: input centerline nodes→migrate centerline nodes→remove cut off nodes→insert or remove nodes to maintain grid spacing→advance time step. The corresponding algorithm to track atoms would then be input cutoff indices→adjust cutoff indices for spacing insertions/removals→adjust cutoff indices for cutoffs removed upstream→"advance" to previous time step. The specifics of the accounting algorithm are dependent on the model implementation; for example, some models may smooth the centerline near a cutoff and if this process adds or removes nodes, the accounting scheme must consider it.

As the algorithm tracks cutoff nodes backward through time, the atom being tracked shrinks. At some point the tracked atom reaches a minimum length associated with its inception or birth, and at this point the algorithm should halt. If the algorithm instead continues tracking, the tracked cutoff indices become meaningless as they represent a part of another atom whose cutoff gave birth to the originally tracked atom. Therefore a threshold on the atom's change in length serves as a robust method to identify time of inception: i.e., abort tracking when $L_a(j) - L_a(j-1) > L_{\text{thresh}}$, where j refers to the jth iteration of the tracking algorithm for a particular atom. We recommend $L_{\text{thresh}} = 10B$ based on the modeling scheme herein, but this threshold depends on the strategy implemented to enforce sufficient node spacing.

3.2. Limitation of the Methodology

The atom extraction scheme cannot be applied to a model which periodically regrids the centerline. Generally, node spacing can be maintained by either globally regridding the full centerline or adding or removing nodes locally. Both methods require an interpolation scheme, usually parametric cubic splines [*Duris*, 1977; *Legleiter and Kyriakidis*, 2007], which invariably introduces errors into the channel centerline [*Crosato*, 2007]. The atom tracking algorithm presented here cannot be used in conjunction with global regridding because regridding erases the individual node history exploited by the algorithm. While most meander migration models do regrid the channel centerline periodically [e.g., *Duan and Julien*, 2010; *Posner and Duan*, 2012; *Motta et al.*, 2012b], it is not required generally. (*Camporeale et al.* [2005] do take advantage of equal node spacing for coordinate transformation and cutoff detection.) While some smoothing is usually required for stability, local interpolation introduces fewer errors into the centerline configuration compared with complete regridding. Moreover, regridding essentially low-pass filters the channel centerline at a frequency determined by the interpolation scheme, removing the smallest-scale bends [*Crosato*, 2007]. Modelers have successfully employed local interpolation schemes (*Sun and Meakin* [1996]; *Sun et al.* [2001], model herein), avoiding the need for computationally-expensive regridding schemes while maintaining spacing requirements and numerical stability.

However, even local regridding poses a problem for the algorithm: as a bend grows and nodes are added, sometimes the interpolated node becomes the cutoff node being tracked. In other words, an atom's cutoff node(s) may not have existed at the atom's inception but were interpolated during its growth. In this case, when tracking an atom's two cutoff nodes backward through time, this node disappears at the time step it was originally introduced (Figure 4). Rather than halt the algorithm, the node nearest the one removed

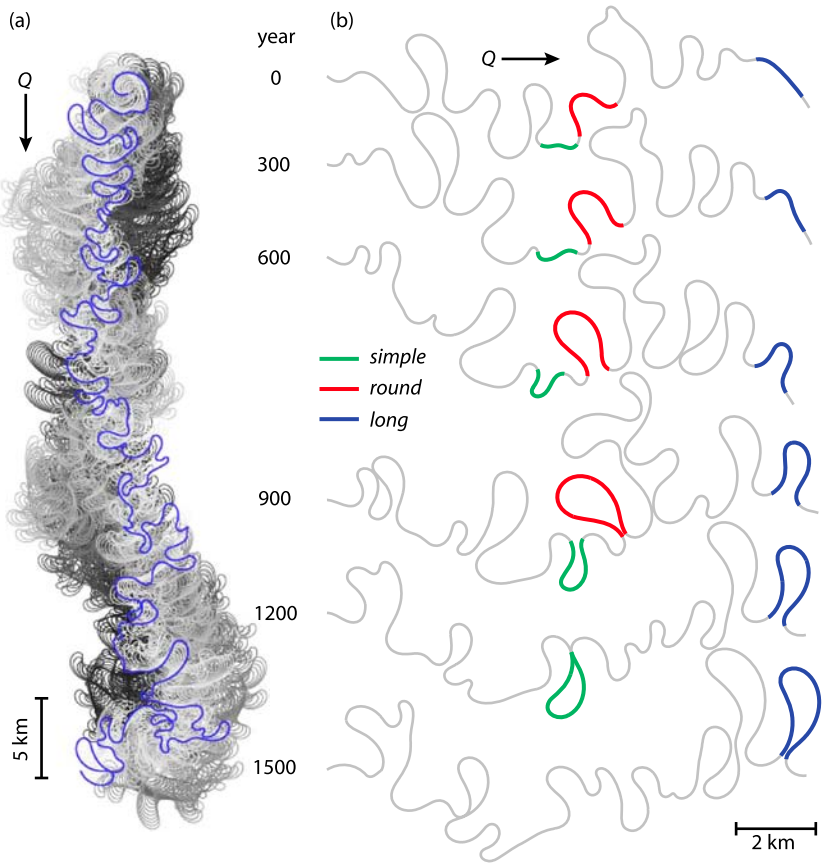

Figure 5. Results of the long-term simulated meandering river. (a) 30,000 years of modeled centerline realizations. Older centerlines are darker; the blue centerline shows $t = 30,000$ years. The upstream boundary condition fixes the first centerline node in place, leading to the formation of the spiral pattern at the upstream boundary. No restrictions are placed on the downstream node so the river may migrate freely. (b) A reach of simulated centerline selected shows the growth and cutoff of all three atom types. Realizations are 300 years apart. Note the complex multilobe meander that starts as double lobed but develops a third lobe before cutting off between 900 and 1200 years.

becomes the cutoff node at the next time step. The frequency of such instances depends on the average node migration rates (which depend on model parameters) and the spacing thresholds, but for the simulation herein this occurred approximately once per atom lifetime.

4. Results

The simulation of a slightly perturbed, initially straight 40 km river reach for 30,000 years (Figure 5a) resulted in 992 cutoffs corresponding to one cutoff approximately every 30 years. Of these 992 atoms, only those occurring a downstream distance greater than 20% of the entire reach length were considered further, ensuring that atom dynamics are unaffected by the upstream periodic boundary condition on curvature (see section 2.2.2). Our model allows only downstream propagation of perturbations so the threshold was not applied to the downstream portion of the reach. The mean tortuosity, or ratio of river length to the distance between its ends, approached a steady average value of 4.46 after 3000 years, and atoms occurring before this time were not included in the analyses. Of the remaining atoms, only those with life spans longer than 400 years were considered to ensure sufficiently long time series, leaving a total of 672 atoms. The following results draw only from these 672 atoms unless otherwise noted.

This section contains three parts that describe the lifetime of an atom. In section 4.1, atom cutoff geometries are classified and geometric relationships established; three archetypal emergent cutoff shapes are identified and compared. In section 4.2, atoms' dynamic histories are described using three measures

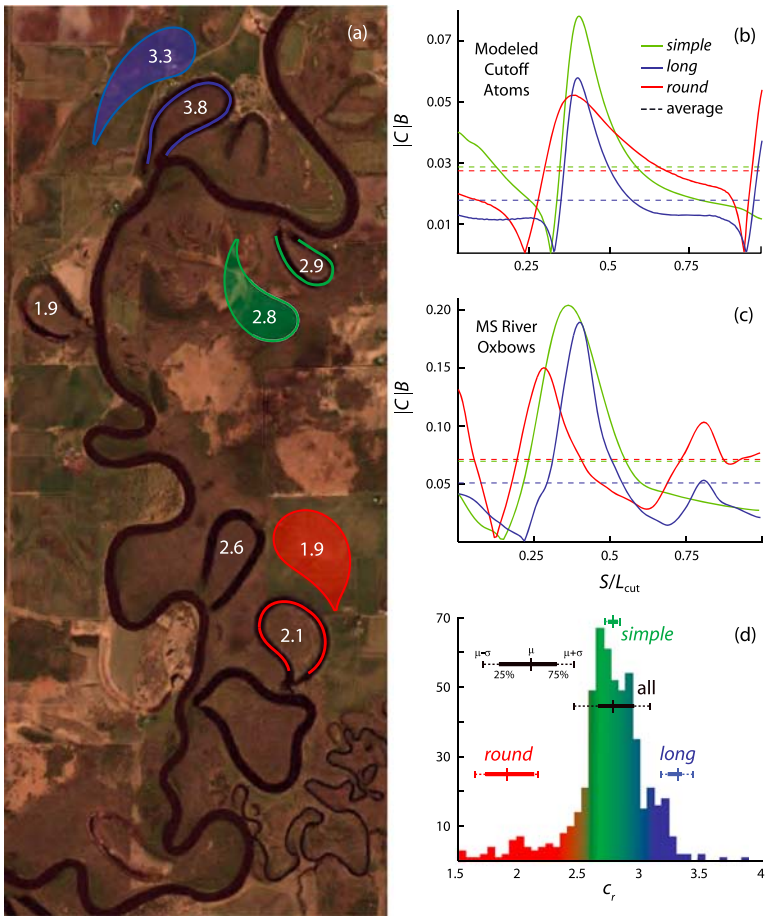

Figure 6. Geometric classification via curvature measures of modeled and real meander loops. (a) Aerial imagery of a reach of the Mississippi River in Minnesota, USA. Centerlines of three oxbows have been traced in colors corresponding to the cutoff atom geometry they most resemble. The shaded meander loops are cutoff atoms simulated by the model and are positioned next to similarly shaped oxbows. White numbers in the center of each oxbow or atom are c_r values. (b) Absolute value of curvature signals for the cutoff atoms simulated by the model shown in (a). Dashed lines are average absolute curvatures. (b) Absolute value of curvature signals for the traced oxbow lakes of the Mississippi River shown in (a). (c) The distribution of c_r (ratio of apex curvature to average curvature) simulated by the model shows how c_r serves as a good metric for ordering meander loops of various geometries by shape. The color gradient of the c_r histogram emphasizes that simulated atom shapes are characterized by a spectrum rather than falling neatly into one of the three archetypal shape (*simple, round, long*) categories. Statistics for each group have sample size $n = 25$, while $n = 552$ for all cutoff atoms. The c_r mean value for all cutoff atoms is 2.77. Map data: *Google Earth: DigitalGlobe.* 46°37′31.36″N, 93°38′13.31″W. Imagery date 7/2/2011.

of bend-scale meander dynamics. Finally, in section 4.3, the results from the preceding two sections are combined to demonstrate that cutoff geometry contains the signature of historic formative dynamics.

4.1. Atom Cutoff Geometries

Atom cutoff geometries emerging from the simulation spanned a variety of planform shapes and sizes including double- and triple-compound loops and a diversity of single-lobed bends. Despite this diversity, some recurring archetypal cutoff atom shapes were identified through basic curvature and shape metrics. In general, the inability of HIPS models to reproduce the resonance phenomenon and hence failure to describe superresonant conditions produces single-lobed bends that are invariably upstream skewed and downstream migrating [*Lanzoni and Seminara*, 2006].

Following *Brice* [1974], we first separated *singles* from *multilobes* requiring that a *single* have a maximum of two inflection points and only one maximum curvature corresponding to the apex of the bend (e.g., Figure 3b, left). By this criterion 82% of all atoms were singles. *Multilobe* atoms (e.g., Figure 3b) showed substantial variability in their planform geometries that precluded analysis using the metrics developed

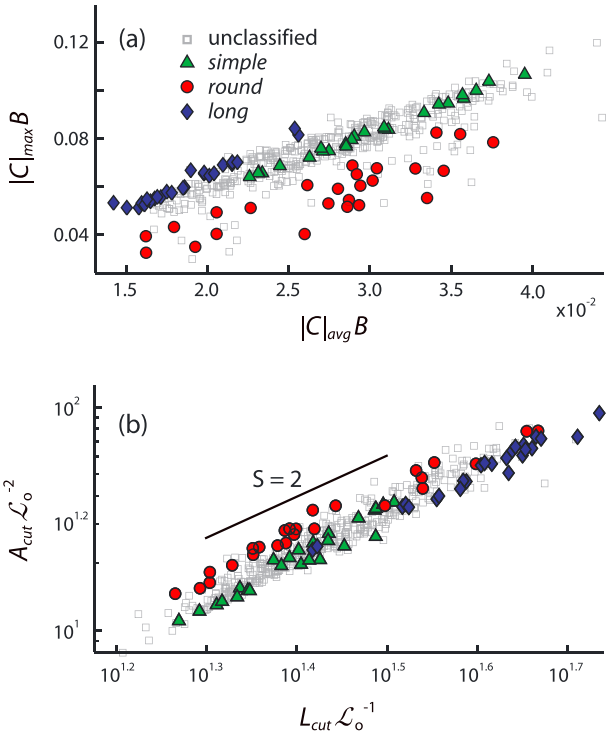

Figure 7. Geometric phase spaces for all single atoms at cutoff. (a) Relationship between mean and maximum absolute curvatures for each single cutoff atom made dimensionless by channel width. Each symbol represents a unique cutoff atom geometry. The shape groups tend to follow straight lines because shape classifications were based on the approximately constant ratio $|C|_{max}/|C|_{avg}$. (b) Log-log relationship between cutoff length L_{cut} and area A_{cut} for each single cutoff atom. Area and length are nondimensionalized with $\mathcal{L}_o$, the length scale relevant to meander migration described in section 4.2. For a given cutoff length L_{cut}, *rounds* tend to cover a larger area whereas *simples* and *longs* occupy approximately the same area. The average slope of the marker cloud is two, since $A \sim L^2$ for nonfractal geometries.

here. The hydrodynamic model we employ contains no inherent dynamic mechanisms capable of forming a multilobed atom in the absence cutoff perturbations, contrary to models like that of *Frascati and Lanzoni* [2009], for example, which simulates single lobes that grow additional bends before cutoff (their Figure 7a). We therefore consider multilobes produced by the HIPS model as aggregations of individual singles, and subsequently focus our attention solely on singles.

Among the diversity of single planform configurations, three archetypal shapes emerged from the simulation dubbed here as *simple*, *round*, and *long* (Figure 6a). We note that these shape designations are presented as a conceptual model to help relate different geometries to distinct dynamic behavior and not intended as a broader classification scheme. *Simple* cutoff atoms have a teardrop shape reminiscent of the classic *Kinoshita* [1961] loop. *Simples* are prototypical in the sense that in the absence of large perturbations (i.e., an initially straight planform with only small perturbations in curvature), they are the only shape that forms. Indeed, each of the first 30 cutoffs of the simulation fell into the *simple* category. The spectrum of *simples* ranges from a fatter planform shape (*round*), to an elongated version (*long*), both of which may be considered stretched *simples*. *Longs* are stretched parallel to the long axis of the meander loop, while *rounds* are stretched in the perpendicular direction.

The previously qualitatively described classifications may also be distinguished quantitatively by considering the ratio of the absolute curvature at the apex of an atom to the average absolute curvature along the cutoff atom $c_r = |C|_{max}/|C|_{avg}$ (Figure 6d). This dimensionless ratio, which is unity for a circle, clusters similarly shaped cutoff atoms together such that those atoms with values near the mean tend toward the *simple* shape, while atoms with values closer to one have *round* geometry (Figure 6d). For larger values of the ratio, cutoff atoms become more elongated giving rise to the *long* group. To illustrate the links between geometric and dynamic relationships, we selected 25 cutoff atoms with the lowest (highest) c_r values to represent *rounds* (*longs*) and chose 25 cutoff atoms nearest the mean c_r value to represent *simples*. As Figure 6b shows, both the maximum and average curvature values are necessary to distinguish between the three groups; the $|C|_{max}$ value for the *round* cutoff atom is very near the *long* cutoff atom, but their $|C|_{avg}$ are dissimilar. For the *round* and *simple* cutoff atoms, the situation is reversed and the $|C|_{avg}$ values are close but the $|C|_{max}$ values differentiate the two.

Regardless of their stage of development at cutoff and despite the various centerline configurations, simulated single cutoff atoms' apex curvatures scale linearly with their average curvatures depending on shape (Figure 7). The cutoff atom groupings in Figure 7 reflect the use of c_r as a metric; each group maintains approximately the same ratio and therefore falls within a narrow band. *Rounds* exhibit significantly more

geometric variability than other types. For example, for a given $|C|_{avg}$ the range of observed $|C|_{max}$ is greater for *rounds* than *longs*. A cutoff atom's area scales with the square of its perimeter as with nonfractal 2-D polygons.

4.2. Atom Dynamics

The complex behavior of meandering river migration has given rise to a host of metrics designed to capture the many possible planform migration modes of a meander bend [e.g., *Brice*, 1974, *Lagasse et al.*, 2004]. Here we take advantage of the atom extraction algorithm which delineates a meander loop through time along with known simulated migration at every point and time and investigate atom evolution via three migration measures: average migration rate (φ_{avg}), centroid migration rate (φ_{cen}), and atom growth rate ($\frac{dL_a}{dt}$).

4.2.1. Dynamic Measures

A single node's instantaneous migration rate is computed as the Euclidian distance between the node's location after some elapsed time divided by the elapsed time:

$$\varphi_i(t) = \frac{1}{\triangle t} \left\| \begin{matrix} X_i(t+\triangle t) - X_i(t) \\ Y_i(t+\triangle t) - Y_i(t) \end{matrix} \right\|_2 \tag{7}$$

for some node i, where $\|\mathbf{x}\|_2$ is the Euclidian norm of $\mathbf{x}$.

Average migration rate φ_{avg} is simply the average of all an atom's nodes' migration rates (weighted by node spacing) at a given time, or

$$\varphi_{avg}(t) = \frac{1}{L_a} \sum_{i=1}^{m} \triangle S_i \varphi_i \tag{8}$$

where $L_a = \sum_{i=1}^{m} \triangle S_i$ is the atom length, m is the number of nodes comprising the atom, and $\triangle S$ was found by first-order differencing. Average migration condenses the local migration activity along a meander loop into a single measure.

Centroid migration rate, φ_{cen}, considers the movement of the centroid of the polygon formed by joining an atom's cutoff nodes with a line segment. Equation (9) specifies the centroid coordinates of a polygon composed of m nodes computed from its moments of inertia.

$$\begin{aligned} X_C &= \frac{1}{6} \sum_{i=1}^{m} \frac{6x_i y_i \Delta x_i - 3x_i^2 \Delta y_i + 3y_i \Delta x_i^2 + \Delta x_i^2 \Delta y_i}{y_i \Delta x_i - x_i \Delta y_i} \\ Y_C &= \frac{1}{6} \sum_{i=1}^{m} \frac{-6x_i y_i \Delta y_i + 3y_i^2 \Delta x_i - 3x_i \Delta y_i^2 - \Delta y_i^2 \Delta x_i}{y_i \Delta x_i - x_i \Delta y_i} \end{aligned} \tag{9}$$

where $\Delta x_i = x_{i+1} - x_i$, $x_m = x_0$ and $\Delta y_i = y_{i+1} - y_i$, $y_m = y_0$. The centroid migration rate φ_{cen} is then computed by equation (7) with $(X_i, Y_i) = (X_C, Y_C)$. Computed as such, the centroid migration rate is an integrated measure of all modes of atom migration, i.e., translation, rotation, extension, and expansion [*Daniel*, 1971]. For example, downstream translation of an atom and streamwise-perpendicular growth of the atom may have similar centroid migration rates yet result in significantly different atom planform shapes.

Atom growth rate ($\frac{dL_a}{dt}$) simply measures the rate of change of length:

$$\frac{dL_a}{dt}(t) = \frac{L_a(t+\triangle t) - L_a(t)}{\triangle t} \tag{10}$$

for some atom a.

Migration rates are normalized by the space scale ($\mathcal{L}_o$) and time scale (τ_o) characterizing the length growth rate that emerges naturally from the structure of the solution for excess bank velocity given by equation (2) and from the differential equations controlling migration of the channel axis given by equations (3) and (4). They read $\mathcal{L}_o = B/|\lambda_o| = D_o/2C_{fo}$ and $\tau_o = \mathcal{L}_o/E_o U_o$. The former essentially controls the exponential decay of spatial disturbances of the flow field [*Camporeale et al.*, 2005] and in the subresonant regime has been found to attain values similar to the morphodynamic length scale emerging from more refined models [*Frascati and Lanzoni*, 2009]. The latter is simply dictated by the equation describing how the centerline evolves in time and the bank erosion law.

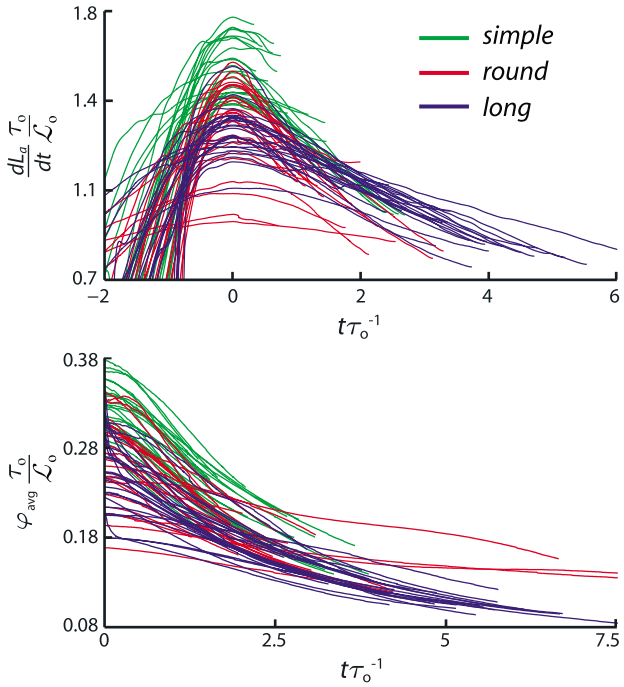

Figure 8. Collections of individual atoms' dynamic trajectories. (a) Atom growth rates $\frac{dL_a}{dt}$. Each trajectory represents the evolution of a single atom's growth rate from near inception until cutoff. The right end of each trajectory corresponds to cutoff. Trajectories are aligned as described in section 4.2 such that their maxima occur at $t=0$ for comparison purposes. (b) Average atom migration rates φ_{avg}. Again, atoms are aligned such that their maxima correspond to $t = 0$. Colors correspond to the shape groups defined in section 4.1. *Simples* and *longs* are well-distinguished but *rounds* exhibit significant variability.

4.2.2. Dynamic Trajectories

As an atom evolves in time, its dynamic trajectory is recorded by the set of dynamic measures describing its evolution. Here we show how average migration rate, centroid migration rate, and length growth rate change in time for individual atoms of each type of cutoff shape (i.e., *round, simple*, or *long*) and characterize the variability of dynamic trajectories simulated by our HIPS model. Despite a substantial variability in dynamic signals, a significant connection is demonstrated between cutoff geometry and dynamics.

Near inception, atom length growth rates $\left(\frac{dL_a}{dt}\right)$ remain slow but increase until eventually reaching a maximum growth rate and then monotonically decreasing (Figure 8a). The trends in the modeled growth rate trajectories agree with both field observations [*Nanson and Hickin*, 1983] and theoretical analyses [*Seminara et al.*, 2001]. Empirically, the amplitude growth rate of real single bends typically rises to a peak before decreasing, while its migration speed decreases monotonically [*Nanson and Hickin*, 1983]. Theoretically, the nonlinear solution of the integrodifferential equation governing the planimetric evolution of a periodic sequence of meanders indicates that early in a meander's life, the fundamental harmonic (that is, the sine-generated curve of *Langbein and Leopold* [1966]) grows linearly. After this phase, the third harmonic (represented in the Kinoshita curve) is also excited leading to a nonlinear meander growth that progressively retards. As a result, the meander growth rate increases slowly during the linear phase, attains a maximum and then decreases as the third harmonic is activated. Additionally, the downstream-migration rate is found to decrease to very small values before cutoff while the rate of bend amplification grows to a peak and then decays slowly. As this evolution takes place, the meander progressively fattens and becomes skewed upstream due to the growth of the third harmonic.

An atom's average migration rate is greatest near its inception, but similar to growth rate, it monotonically decreases after attaining a maximum (Figure 8b). The peaks in average migration rate trajectories occur well before those in growth rate trajectories, rendering them useful metrics of historic dynamics. Note that the time axes in Figure 8 are not identical; because inception and cutoff are not standard across all atoms, the dynamic trajectories were aligned such that their peaks occur at $t=0$ to establish a benchmark for meaningful comparisons between trajectories. Average migration rate trajectories for *simple* and *long* atoms occupy distinct regions, with *simples* exhibiting higher rates. As with geometric variability, *rounds* also display more dynamic variability than other atom shapes.

The irregularity of centroid migration trajectories prohibits meaningful presentation of their dynamic trajectories as shown for average migration and length growth rates in Figure 8, but the centroid migration rate nevertheless provides a different perspective on the connection between dynamics and geometry. This rate (φ_{cen}, Figure 9a) is evidently connected with the anatomy of an atom which is divisible into two distinct parts: a head and tail(s). An atom's head is the reach of atom containing the apex of the bend between two inflection points. Heads roughly correspond to the classic notion of a meander bend as the reach of a river between inflection points. Tails are simply the portions of the atom that are not its head. As shown

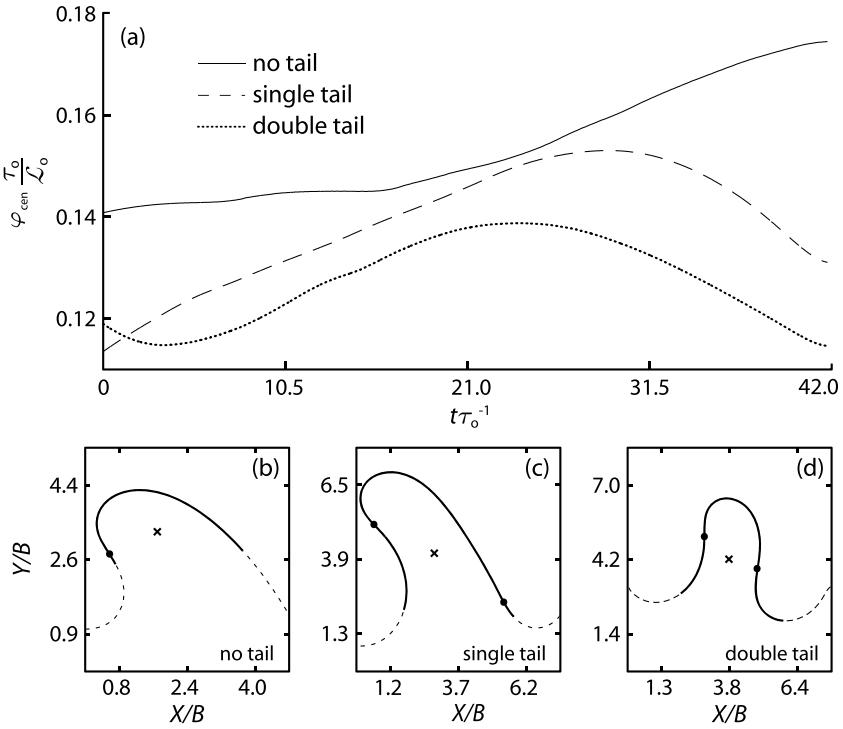

Figure 9. The effect of tails shown via centroid migration rates φ_{cen} through time for the three atom centerlines. See section 4.2.2 for interpretation. (a) Cutoff occurs at $t/\tau_o = 42.0$. (b–d) The planforms for each of the atoms of different tail types are plotted at $t = 0$. The solid black lines are the atoms and the continuing dashed line is the river centerline. The black dots in (b–d) show the inflection points for each atom centerline, and the crosses mark the centroid of each atom.

in Figures 9b– 9d, an atom may have zero, one, or two tails. The tails of an atom can contain the apex of a less-developed (hence faster migrating, see Figure 8b) adjacent loop; the high curvatures of such nearby loops induce faster migration of tails compared to their corresponding heads. The presence of tails dramatically affects the centroid migration rate (Figure 9a) and generally acts to diminish φ_{cen} magnitudes. For example, the tailless atom in Figure 9b has the fastest φ_{cen} among the three types; φ_{cen} diminishes with an increased number of tails. This effect of tails is perhaps unsurprising, as tails add weight opposite to the direction of apex growth thereby suppressing the outward migration of the centroid. Interestingly, tails also influence φ_{cen} by imparting a local maximum into the signal (Figure 9a, single and double tails) corresponding to their migration toward cutoff. As tails migrate toward each other, they begin to straighten. The peaks in φ_{cen} correspond to the straightening of the tails (i.e., tails approaching smaller $|C|_{avg}$) which acts to significantly reduce the weight of the tails on the centroid location. Not only is the magnitude of φ_{cen} dependent on tail behavior, the timing of its maximum (i.e., max (φ_{cen})) also depends on the number of tails; more tails lead to earlier peaks (relative to time of cutoff).

The three dynamic measures show different aspects of an atom's evolution, but they are not independent of each other. Average migration rate peaks shortly after inception and then monotonically decreases until cutoff, whereas the growth rate is small near inception and grows to a maximum value before decreasing until cutoff. A typical *simple* atom (Figure 10) shows that the occurrence of these maximum or minimum dynamic metrics is not simultaneous. Average migration and centroid migration appear correlated until the tails of the atom begin affecting the centroid migration rate, causing its rise despite the decreasing overall average migration rate. Despite some apparent correlation, each measure provides unique information about the modes of planform migration.

4.3. Connecting Geometry and Historic Dynamics

A meander loop's dynamics arise from the continuous feedbacks between the morphodynamic, hydrodynamic, and geometric processes at play, and its planform shape bears the signature of their interaction. The

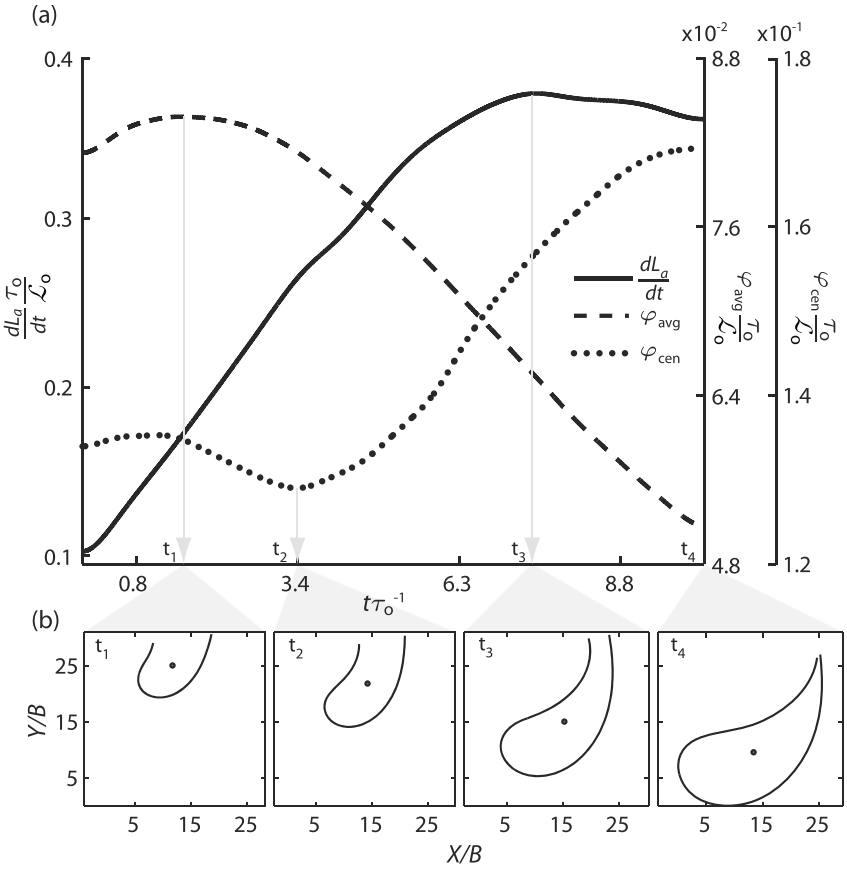

Figure 10. How dynamic metrics simultaneously evolve for a single atom. (a) The evolution of a typical *simple* atom is visualized through three dynamic measures changing in time: growth rate (solid line), average migration rate (dashed line), and centroid migration rate (dotted line). Dynamic measures are nondimensionalized by the time and space scales described in section 4.2. Vertical lines are drawn from each of the dynamic signals' local maxima or minimum to their times on the *x* axis. (b) The atom's planform is shown plotted at each of these times (t_4 corresponds to cutoff). The dot inside each of the plotted atom centerlines shows the atom's centroid. After t_2 the left tail of the atom begins rapidly migrating toward the right causing the rebound of φ_{cen} and the atom's eventual cutoff.

relationship between a meander bend's curvature and dynamics (i.e., migration rates) has been explored in both real [*Hickin*, 1974; *Hickin and Nanson*, 1975; *Hooke*, 1987, 2007] and simulated [*Crosato*, 2009] channels, but these studies only consider instantaneous relationships. If meander bends remember their formative dynamics, a connection should exist between the bend's current planform configuration and the dynamic history that brought it to that state. This hypothesis, that the signature of formative dynamics remains in cutoff shapes, is tested using the methodologies developed in the previous two subsections.

A simple linear correlation analysis between each atom's maximum average migration rate and more than 30 metrics of cutoff atom geometry revealed the two strongest correlating variables are the efficiency ratio A_{cut}/L_{cut} (Figure 11a), which refers to how efficient an atom's centerline length at cutoff was in reworking the floodplain, and the apex curvature at cutoff $|C|_{max}$ (Figure 11b). This is perhaps an unsurprising result considering the work of *Furbish* [1988] who showed that within a HIPS-type model both curvature and stream length are of similar importance to meandering river migration dynamics. The consideration of both efficiency ratio and apex curvature improved predictions of maximum average migration rate (Figure 12). Maximum growth rates and maximum centroid migration rates produce similar results to Figure 12; that is, cutoff atom geometry predicts all three dynamic metrics well. However, because an atom's maximum average migration occurs very early in its life (see Figure 12), it provides the earliest measure of its dynamics and implies that the geometry at the end of an atom's life contains information about its dynamics near the time of its inception. Furthermore, the signature of formative dynamics in cutoff shapes supports the

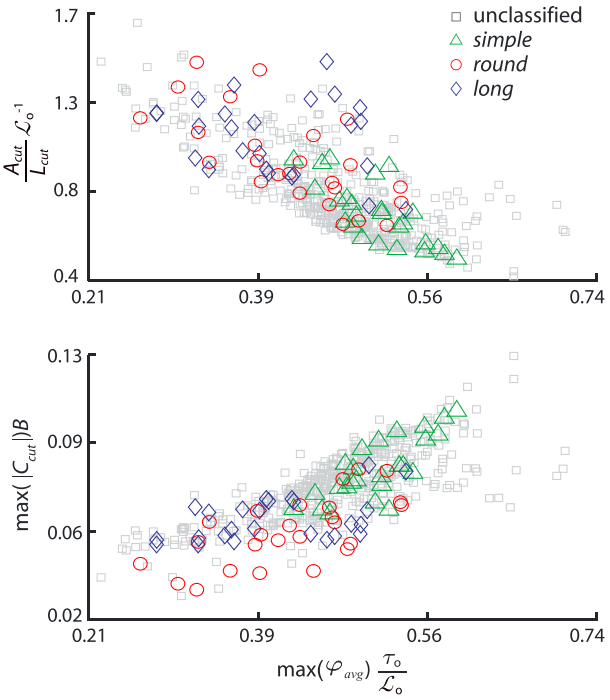

Figure 11. Relationships between cutoff geometry and historic dynamics for 552 *simple* cutoff atoms. (a) The efficiency ratios A_{cut}/L_{cut} normalized by $\mathcal{L}_o$ for all cutoff atoms are plotted against their maximum average migration rates (shown in Figure 8b). Efficiency ratio refers to the efficiency of a given length of stream in reworking the floodplain. (b) Each cutoff atom's apex curvature normalized by B is plotted against its historic maximum average migration rate.

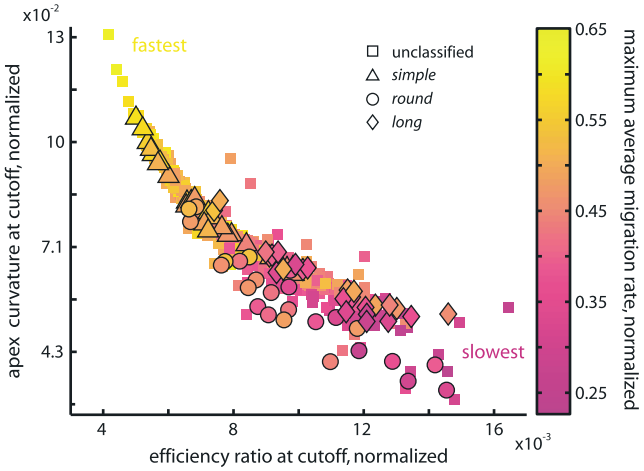

Figure 12. Connection between cutoff geometry and historic dynamics revealed. Measurements of atom geometries (x and y axis) at the end of each atom's life and a measure of their dynamics (coloration) made early in the atom's life link an atom's dynamic history with its cutoff shape. For each atom the dimensionless efficiency ratio at cutoff $A_{cut}/L_{cut}\mathcal{L}_o^{-1}$ is plotted against the dimensionless apex cutoff curvature $\max(|C|_{max})B$ and the point is colored by the dimensionless historic maximum average migration rate, $\max(\varphi_{avg})\tau_o/\mathcal{L}_o$ (i.e., the maxima of trajectories shown in Figure 8b). The fastest migrating atoms correspond to those with the highest apex curvatures and lowest efficiency ratios (top left) and vice versa.

notion of a critical period early in a meander bend's life when its dynamic trajectory is most sensitive to perturbation. Deviations from the apparent trend in Figure 12 are mostly due to cutoffs occurring immediately upstream. Such cutoffs serve as high-curvature perturbations that may migrate downstream into the upstream-tail of an atom, and the maximum migration rate is amplified when this perturbation coincides with the peak growth rate of the downstream atom. Consistent with geometric and dynamic metrics, *rounds* exhibit the most variability in the predictive relationship between cutoff geometry and dynamics.

5. Discussion

The life story of meander bends predicted by a HIPS formulation is told through their extraction as atoms. An atom undergoes a birth and death, and its anatomy is composed of a head corresponding to the reach of centerline containing the apex of the bend between two inflection points and tails corresponding to the lengths of stream between the inflection points and cutoff locations. The death of an atom is marked by cutoff, and its timing for a given atom depends on (i) the atom's dynamic history, (ii) nearby perturbations, and (iii) the overall river planimetric configuration. At its birth an atom is usually a mere squiggle of centerline (e.g., Figure 3b) and therefore cannot be easily visually detected. With respect to each of the three dynamic measures, *simple* atoms tend to migrate fastest and hence reach cutoff sooner than other geometries. *Long* atoms migrate the slowest and therefore live the longest before cutoff. The variability in *round* geometries is also seen in their dynamic trajectories, reflecting the influence of randomly timed nearby perturbations due to cutoff. Conversely, *simples* and *rounds* have dynamic trajectories that cluster with smaller variability. Some

atoms' maximum growth rates (see slowest growing *rounds*, Figure 8a) are apparently achieved early in their lives, suggesting that their cutoff geometry is set early in their life. This implies a critical period near inception when perturbations are most critical to development.

In our HIPS model, model dynamics do not include physical mechanisms such as transitions from subresonant to superresonant conditions as described by *Frascati and Lanzoni* [2009], and hence cutoff is the only localized perturbation mechanism through which new meander bends may form. This property, along with uniform treatment of post-cutoff centerline smoothing begs the question: how do the various observed morphodynamics arise? An atom's morphology is determined primarily by the local hydrodynamics driving bank erosion (u_b, equation (2)), but these local dynamics depend on both nonlocal and reach-wide conditions that vary in time. For example, U_o, D_o, and λ_o are reach-wide variables that affect the migration rate of a single node. Furthermore, the convolution integral in equation (2) represents a nonlocal (yet nonreach wide) dependence on upstream curvatures. The hydrodynamics of an atom incorporate the variability from each of these scales and thus promotes variability in individual atom morphodynamics. In addition to variability in local hydrodynamics, the atom deformation process itself imparts an intrinsic geometric nonlinearity through the equations of migration (see *Pittaluga and Seminara* [2011]). The occurrence of cutoff imparts yet another source of variability into the migrating meandering river.

Ultimately, the various emergent atom morphodynamics and morphologies reflect the nonlinear interactions between the multiscale-dependent hydrodynamics, the migration equations, and the occurrence of cutoffs. Even in a relatively simple modeling environment like ours, unraveling the contributions of each of these to specific morphologic or dynamic variability presents a considerable challenge. A comparison of the computed terms contributing to excess bank velocity u_b reveals curvature effects are typically stronger than the slowly varying reach-wide ones especially near cutoffs. That is, local curvature perturbations account for more of the variability in the distribution of shapes shown in Figure 6d; the resulting discontinuity in curvature after cutoff serves as the initial configuration of a new atom. Cutoffs sometimes also clearly affect nearby well-developed atom dynamics through the nonlocal term, usually acting to "artificially" augment migration rates (for example, the outliers in Figure 12). In the absence of localized perturbations, cutoff geometries simulated by the HIPS model tend toward a uniform *simple* shape, suggesting an inherent archetypal form embedded in the model dynamics.

The curvature, area, and length of a meander loop at cutoff can be used to predict historic maximum rates of growth and migration as demonstrated by Figure 12. For example, Figure 6a shows oxbow lakes along the Mississippi River that had already formed at the time of the earliest aerial photographs in 1937; observations of their formative dynamics are unavailable. However, if this reach of the Mississippi River were well-described by a HIPS modeling scheme, historic migration rates of each loop may be estimated from their present-day oxbow c_r ratios. Even without fully modeling the historic evolution of this reach of the Mississippi River, relative migration rates of each oxbow may be inferred from a cursory analysis of their geometries.

The results presented herein were made possible only because the entirety of an atom's life is known, including the cutoff. If the cutoff location and time are known, the rest of the atom's evolution may then be backtracked until its origins and initial conditions are known. The algorithm introduced here requires highly temporally resolved centerline realizations to accurately track cutoff node histories. In principle this algorithm could be applied to cutoff loops from a series of aerial images with sufficient temporal resolution if a consistent method for gridding centerlines were established. Alternatively, adopting the classical notion of a meander bend as the reach of stream between inflection points (i.e., atom heads) would permit the technique's application to real reaches that have not yet been cut off. In that case, the methodology here is still useful because the heads are easily extracted from complete atoms while bypassing the previously discussed problems associated with automatic inflection point detection.

6. Concluding Remarks and Future Work

The primary motivation of this work was to test the hypothesis that bend-scale cutoff geometry contains information about its formative dynamics. Testing this hypothesis requires both a large number of meander bends whose planimetric bend evolutions from inception until cutoff are well-resolved and a record of nearby disturbances that might affect the geometric-dynamic predictive relationship due to the nonlinear

growth of local instabilities. In the absence of sufficient observational data, we resorted to a long-time, physically based numerical model that couples hydrodynamics, morphology, and cutoff and found that the deterministic model dynamics do indeed show evidence that meander cutoff shape contains the signature of formative meander migration dynamics. A necessary step for such an analysis requires the isolation of individual bends through time, and this work presented a robust algorithm to automatically extract single bends from long-time simulations of meander migration.

The ultimate objective, of course, is to apply these findings to real meander bends where "signature-shredders" [*Jerolmack and Paola*, 2010] such as catastrophic floods or geologic activity may obscure or erase this signature. A critical component of such studies lies in the ability to discern which dynamic and geometric metrics might be most closely related. Limited observed meander dynamics data obscured by natural heterogeneities renders identifying such metrics problematic. Within the sterile modeling environment of this work, the apex curvature of cutoff meander bends and the efficiency ratio, defined as the area of a cutoff bend divided by its length, emerge as powerful geometric metrics that retain information about a bend's dynamics in its formative (early) stage of life. Furthermore, maxima of dynamic trajectories serve as suitable metrics characterizing atoms' historic evolutions. Informed by these clues from numerical modeling, future work will test the metrics and relationships developed here in real rivers such as highly active meandering Amazonian rivers for which over 30 years of Landsat imagery is available. We are also applying and refining our metrics to more complex numerical models which incorporate additional physics and natural variability.

Notation

A	slope factor $= \alpha + 1$.
A_a, A_{cut}	atom area [L^2], atom cutoff area [L^2].
B	channel half width [L].
C, c	curvature $= 1/R$ [L^{-1}], nondimensional curvature $= CR_o$.
$\lvert C\rvert_{\text{avg}}$	mean absolute curvature [L^{-1}].
$\lvert C\rvert_{\text{max}}$	maximum absolute curvature between two inflection points (at bend apex) [L^{-1}].
C_{fo}	friction coefficient.
c_r	ratio of maximum curvature to mean curvature $= \lvert C\rvert_{\text{max}}/\lvert C\rvert_{\text{avg}}$.
D, D_o	channel depth [L], reach-averaged channel depth $= \left(Q_o/\left(2B\sqrt{gs_o/C_{fo}}\right)\right)^{2/3}$ [L].
$\frac{dL_a}{dt}$	atom length growth rate (equation (10)) [LT^{-1}].
E_o	erodibility coefficient.
F_o	reach-average Froude number $= U_o^2/D_o g$.
g	gravity acceleration [LT^{-2}].
L_a, L_{cut}	atom length [L], atom cutoff length [L].
$\mathcal{L}_o$	spatial scale governing long-time meander migration $= B/\lvert\lambda_o\rvert$ [L].
m	number of nodes comprising channel centerline.
N, n	cross-stream distance [L], nondimensional cross-stream distance $= N/B$.
Q_o	streamflow [L^3T^{-1}].
R, R_o	radius of curvature (equation (5)) [L], minimum R for reach of interest [L].
S, s	along-stream distance [L], nondimensional along-stream distance $= S/B$.
$s_o(t=0), s_v$	initial channel slope, valley slope.
$t, t_{\text{cut}}, t_{\text{peak}}$	time [T], time at cutoff [T], time of peak (or valley) in dynamic trajectory [T].
U_b, u_b	excess bank velocity (equation (2)) [LT^{-1}], nondimensional excess bank velocity $= U_b/U_o$.
U_o	reach-averaged channel velocity $= Q_o/2BD_o$ [LT^{-1}].
α	transverse bed slope parameter.
β	aspect ratio $= B/D_o$.
ζ_i	migration rate at node i (equation (1)) [LT^{-1}].
θ	angle between valley and streamwise directions (see Figure 1) [rad].
κ_i	curvature computed by ith method (see section 2.2.2) [L^{-1}].
λ_o	characteristic exponent $= -2\beta C_{fo}$.
ν_o	ratio of half width to radius of curvature$= B/R_o$.

ξ dummy variable for convolution integral (equation (2)).
τ_o temporal-scale governing long-time meander migration = $\mathcal{L}_o/E_oU_o$ [T].
φ, φ_{cen}, φ_{avg} migration rate (equation (7)) [LT^{-1}], centroid migration rate (equations (7) and (9)) [LT^{-1}], average migration rate (equation (8)) [LT^{-1}].

Acknowledgments
This work was supported in part by an NSF Graduate Research Fellowship to the first author, an NSF Water Sustainability and Climate Award (grant EAR-1209402), and an NSF International Award for Science Across Virtual Institutes (SAVI): LIFE (Linked Institutions for Future Earth) (grant EAR-1242458). Efi Foufoula-Georgiou acknowledges the support of the Joseph T. and Rose S. Ling Endowed professorship. Special thanks to Janet Hooke, Guido Zolezzi, an anonymous reviewer, and the Editor Alex Densmore whose comments led to an improved final manuscript. Thanks also to Jonathan A. Czuba for assisting with the figure design. Aerial photography data may be accessed via Google Earth; all other analyses are simulated and may be replicated via Codes S1 in the supporting information.

References

Allen, J. (1965), A review of the origin and characteristics of recent alluvial sediments, *Sedimentology*, *5*, 89–191, doi:10.1111/j.1365-3091.1965.tb01561.x.
Asahi, K., Y. Shimizu, J. M. Nelson, and G. Parker (2013), Numerical simulation of river meandering with self-evolving banks, *J. Geophys. Res. Earth Surf.*, *118*, 2208–2229, doi:10.1002/jgrf.20150.
Baker, V. R., R. C. Kochel, and P. C. Patton (1987), *Flood Geomorphology*, John Wiley, New York.
Beschta, R. L., and W. J. Ripple (2012), The role of large predators in maintaining riparian plant communities and river morphology, *Geomorphology*, *157*, 88–98, doi:10.1016/j.geomorph.2011.04.042.
Blanckaert, K., and H. J. de Vriend (2010), Meander dynamics: A nonlinear model without curvature restrictions for flow in open-channel bends, *J. Geophys. Res.*, *115*, F04011, doi:10.1029/2009JF001301.
Blondeaux, P., and G. Seminara (1985), A unified bar-bend theory of river meanders, *J. Fluid Mech.*, *157*, 449–470, doi:10.1017/S0022112085002440.
Bolla Pittaluga, M., G. Nobile, and G. Seminara (2009), A nonlinear model for river meandering, *Water Resour. Res.*, *45*, W04432, doi:10.1029/2008WR007298.
Brice, J. (1974), Evolution of meander loops, *Geol. Soc. Am. Bull.*, *85*(4), 581–586, doi:10.1130/0016-7606(1974)85<581.
Camporeale, C., P. Perona, A. Porporato, and L. Ridolfi (2005), On the long-term behavior of meandering rivers, *Water Resour. Res.*, *41*, W12403, doi:10.1029/2005WR004109.
Camporeale, C., P. Perona, A. Porporato, and L. Ridolfi (2007), Hierarchy of models for meandering rivers and related morphodynamic processes, *Rev. Geophys.*, *45*, RG1001, doi:10.1029/2005RG000185.
Camporeale, C., E. Perucca, and L. Ridolfi (2008), Significance of cutoff in meandering river dynamics, *J. Geophys. Res.*, *113*, F01001, doi:10.1029/2006JF000694.
Carson, M. A., and M. F. Lapointe (1983), The inherent asymmetry of river meander planform, *J. Geol.*, *91*, 41–55.
Constantine, C. R., T. Dunne, and G. J. Hanson (2009a), Examining the physical meaning of the bank erosion coefficient used in meander migration modeling, *Geomorphology*, *106*(3), 242–252, doi:10.1016/j.geomorph.2008.11.002.
Constantine, J. A., S. R. McLean, and T. Dunne (2009b), A mechanism of chute cutoff along large meandering rivers with uniform floodplain topography, *Geol. Soc. Am. Bull.*, *122*(5-6), 855–869, doi:10.1130/B26560.1.
Coulthard, T. J., and M. J. V. D. Wiel (2006), A cellular model of river meandering, *Earth Surf. Processes Landforms*, *31*(1), 123–132, doi:10.1002/esp.1315.
Crosato, A. (1990), Simulation of meandering river processes, *Communications on Hydraulic and Geotechnical Engineering, No. 1990-03*, TU Delft, Delft, Netherlands.
Crosato, A. (2007), Effects of smoothing and regridding in numerical meander migration models, *Water Resour. Res.*, *43*, W01401, doi:10.1029/2006WR005087.
Crosato, A. (2009), Physical explanations of variations in river meander migration rates from model comparison, *Earth Surf. Processes Landforms*, *34*(15), 2078–2086, doi:10.1002/esp.1898.
Daniel, J. F. (1971), Channel movement of meandering Indiana streams, *USGS Prof. Pap. 732–A*.
de Boor, C. (2001), *A Practical Guide to Splines*, Springer, New York.
Duan, J. G., and P. Y. Julien (2010), Numerical simulation of meandering evolution, *J. Hydrol.*, *391*(1-2), 34–46, doi:10.1016/j.jhydrol.2010.07.005.
Duris, C. (1977), Discrete interpolating and smoothing spline functions, *SIAM J. Numer. Anal.*, *14*(4), 686–698.
Dury, G. (1955), Bed-width and wave-length in meandering valleys, *Nature*, *176*, 31–32, doi:10.1038/176031a0.
Eke, E. C., G. Parker, and Y. Shimizu (2014), Numerical modeling of erosional and depositional bank processes in migrating river bends with self-formed width: Morphodynamics of bar push and bank pull, *J. Geophys. Res. Earth Surf.*, *119*, 1455–1483, doi:10.1002/2013JF003020.
Ferguson, R. (1975), Meander irregularity and wavelength estimation, *J. Hydrol.*, *26*(3-4), 315–333, doi:10.1016/0022-1694(75)90012-8.
Frascati, A., and S. Lanzoni (2009), Morphodynamic regime and long-term evolution of meandering rivers, *J. Geophys. Res.*, *114*, F02002, doi:10.1029/2008JF001101.
Frascati, A., and S. Lanzoni (2010), Long-term river meandering as a part of chaotic dynamics? A contribution from mathematical modelling, *Earth Surf. Processes Landforms*, *35*, 791–802, doi:10.1002/esp.1974.
Frascati, A., and S. Lanzoni (2013), A mathematical model for meandering rivers with varying width, *J. Geophys. Res. Earth Surf.*, *118*, 1641–1657, doi:10.1002/jgrf.20084.
Friedkin, J. (1945), A laboratory study of the meandering of alluvial rivers, *Tech. Rep. May 1945*, U.S. Army Corps Eng. Waterw. Expt. Sta., Vicksburg, Miss.
Furbish, D. J. (1988), River-bend curvature and migration: How are they related?, *Geology*, *16*(8), 752–755, doi:10.1130/0091-7613(1988)016<0752:RBCAMH>2.3.CO;2.
Gay, G. R., H. H. Gay, W. H. Gay, H. A. Martinson, R. H. Meade, and J. A. Moody (1998), Evolution of cutoffs across meander necks in Powder River, Montana, USA, *Earth Surf. Processes Landforms*, *23* (7), 651–662, doi:10.1002/(SICI)1096-9837(199807)23:7<651::AID-ESP891>3.0.CO;2-V.
Graf, N. E. (2008), 50 years of channel change on a reach of the Big Blue River, northeast Kansas, PhD thesis, Univ. of Wyoming, Manhattan, Kans.
Güneralp, I., and B. L. Rhoads (2007), Continuous characterization of the planform geometry and curvature of meandering rivers, *Geog. Anal.*, *40*(1), 1–25, doi:10.1111/j.0016-7363.2007.00711.x.
Güneralp, I., and B. L. Rhoads (2010), Spatial autoregressive structure of meander evolution revisited, *Geomorphology*, *120*(3-4), 91–106, doi:10.1016/j.geomorph.2010.02.010.
Güneralp, I., and B. L. Rhoads (2011), Influence of floodplain erosional heterogeneity on planform complexity of meandering rivers, *Geophys. Res. Lett.*, *38*, L14401, doi:10.1029/2011GL048134.

Güneralp, I., J. D. Abad, G. Zolezzi, and J. M. Hooke (2012), Advances and challenges in meandering channels research, *Geomorphology*, *163*, 1–9, doi:10.1016/j.geomorph.2012.04.011.
Hall, P. (2004), Alternating bar instabilities in unsteady channel flows over erodible beds, *J. Fluid Mech.*, *499*, 49–73, doi:10.1017/S0022112003006219.
Hasegawa, K. (1977), Computer simulation of the gradual migration of meandering channels, in *Proceedings of the Hokkaido Branch*, pp. 197–202, Jpn. Soc. of Civ. Eng.
Henriquez, A., K. Tyler, and A. Hurst (1990), Characterization of fluvial sedimentology for reservoir simulation modeling, *SPE Formation Evaluation*, *5*(3), 211–216, doi:10.2118/18323-PA.
Hickin, E. J. (1974), The development of meanders in natural river-channels, *Am. J. Sci.*, *274*(4), 414–442, doi:10.2475/ajs.274.4.414.
Hickin, E. J., and G. C. Nanson (1975), The character of channel migration on the Beatton River, Northeast British Columbia, Canada, *Geol. Soc. Am. Bull.*, *86*(4), 487–494, doi:10.1130/0016-7606(1975)86<487:TCOCMO>2.0.CO;2.
Hooke, J. M. (1977), An analysis of changes in river channel patterns, unpublished PhD thesis, Univ. of Exeter, Exeter, U. K.
Hooke, J. M. (1984), Changes in river meanders: A review of techniques and results of analyses, *Prog. Phys. Geogr.*, *8*(4), 473–508, doi:10.1177/030913338400800401.
Hooke, J. M. (1987), Changes in meander morphology, in *International Geomorphology, 1986: Proceedings of the First International Conference on Geomorphology*, edited by V. Gardiner, pp. 591–609, John Wiley, Chichester, U. K.
Hooke, J. M. (2003), River meander behaviour and instability: A framework for analysis, *Trans. Inst. Br. Geogr.*, *28*, 238–253.
Hooke, J. M. (2007), Complexity, self-organisation and variation in behaviour in meandering rivers, *Geomorphology*, *91*(3-4), 236–258, doi:10.1016/j.geomorph.2007.04.021.
Hooke, J. M., and C. Redmond (1989), Use of cartographic sources for analysing river channel change with examples from Britain, in *Historical Change in Large Alluvial Rivers*, edited by Petts, G., H. Moller, and A. Roux, pp. 79–93, John Wiley, Chichester, U. K.
Hooke, J. M., and L. Yorke (2010), Rates, distributions and mechanisms of change in meander morphology over decadal timescales, River Dane, UK, *Earth Surf. Processes Landforms*, *35*(13), 1601–1614, doi:10.1002/esp.2079.
Howard, A. D. (1996), Modelling channel evolution and floodplain morphology, in *Floodplain Processes*, pp. 15–62, Wiley, Chichester.
Howard, A. D., and A. T. Hemberger (1991), Multivariate characterization of meandering, *Geomorphology*, *4*(3-4), 161–186, doi:10.1016/0169-555X(91)90002-R.
Ikeda, S., G. Parker, and K. Sawai (1981), Bend theory of river meanders. Part 1. Linear development, *J. Fluid Mech.*, *112*, 363–377.
Imran, J., G. Parker, and C. Pirmez (1999), A nonlinear model of flow in meandering submarine and subaerial channels, *J. Fluid Mech.*, *400*, 295–331, doi:10.1017/S0022112099006515.
Irwin, R. P., R. A. Craddock, and A. D. Howard (2005), Interior channels in Martian valley networks: Discharge and runoff production, *Geology*, *33*(6), 489–492, doi:10.1130/G21333.1.
Jackson, N. D., and C. C. Austin (2013), Testing the role of meander cutoff in promoting gene flow across a riverine barrier in ground skinks (Scincella lateralis), *PloS one*, *8*(5), e62812, doi:10.1371/journal.pone.0062812.
Jefferson, M. (1902), *Limiting Width of Meander Belts*, Natl. Geogr., Wash.
Jerolmack, D. J., and C. Paola (2010), Shredding of environmental signals by sediment transport, *Geophys. Res. Lett.*, *37*, L19401, doi:10.1029/2010GL044638.
Johannesson, H., and G. Parker (1985), Computer simulated migration of meandering rivers in Minnesota, *Tech. Rep.*, Univ. of Minn., Minneapolis.
Johannesson, H., and G. Parker (1989), Velocity redistribution in meandering rivers, *J. Hydraul. Eng.*, *115*(8), 1019–1039, doi:10.1061/(ASCE)0733-9429(1989)115:8(1019).
Kinoshita, R. (1961), An investigation of channel deformation of the Ishikari River, *Tech. Rep.*, Nat. Resour. Div., Minist. of Sci. and Technol. of Jpn., Tokyo.
Kondolf, G. (2006), River restoration and meanders, *Ecol. Soc.*, *11*(2), 42.
Lagasse, P., W. Spitz, and L. Zevenbergen (2003), A methodology and ArcView Tools for predicting channel migration, *ESRI, User Conference Proceedings,* San Diego, Calif.
Lagasse, P., L. W. Zevenbergen, W. J. Spitz, and C. R. Thorne (2004), *Methodology for Predicting Channel Migration*, Transp. Res. Board, Natl. Res. Counc., Fort Collins, Colo.
Langbein, W. B., and L. B. Leopold (1966), River meanders—Theory of minimum variance, *USGS Prof. Pap. 422H*.
Lanzoni, S., and G. Seminara (2006), On the nature of meander instability, *J. Geophys. Res.*, *111*, F04006, doi:10.1029/2005JF000416.
Larsen, E. W., and E. Anderson (2002), The controls on and evolution of channel morphology of the Sacramento River: A case study of River Miles 201-185, *Tech. Rep.*, Univ. of Calif., Davis.
Lazarus, E. D., and J. A. Constantine (2013), Generic theory for channel sinuosity, *Proc. Natl. Acad. Sci. U.S.A.*, *110*(21), 8447–8452, doi:10.1073/pnas.1214074110.
Legleiter, C. J. (2014), Downstream effects of recent reservoir development on the morphodynamics of a meandering channel: Savery Creek, Wyoming, USA, *River Res. Appl.*, doi:10.1002/rra.2824.
Legleiter, C. J., and P. C. Kyriakidis (2007), Forward and inverse transformations between cartesian and channel-fitted coordinate systems for meandering rivers, *Math. Geol.*, *38*(8), 927–958, doi:10.1007/s11004-006-9056-6.
Leighly, J. (1936), Meandering arroyos of the dry southwest, *Geog. Rev.*, *62*, 338–344.
Leopold, L. B., and M. Wolman (1957), River channel patterns: Braided, meandering, and straight, *Tech. Rep.*, U.S. Geol. Surv., Washington, D. C.
Leopold, L. B., and M. Wolman (1960), River meanders, *Geol. Soc. Am. Bull.*, *71*(3), 769–794.
Lewis, G., and J. Lewin (1983), Alluvial cutoffs in Wales and the borderlands, *Spec. Publ. Int. Assoc. Sediment.*, *6*, 145–154, doi:10.1002/9781444303773.ch11.
Lorenz, R. D., et al. (2008), Fluvial channels on Titan: Initial Cassini RADAR observations, *Planet. Space Sci.*, *56*(8), 1132–1144, doi:10.1016/j.pss.2008.02.009.
Luchi, R., G. Zolezzi, and M. Tubino (2011), Bend theory of river meanders with spatial width variations, *J. Fluid Mech.*, *681*, 311–339, doi:10.1017/jfm.2011.200.
Melton, F. A. (1936), An empirical classification of flood-plain streams, *Geog. Rev.*, *26*(4), 593–609, doi:10.2307/209717.
Micheli, E. R., and J. W. Kirchner (2002), Effects of wet meadow riparian vegetation on streambank erosion. 1. Remote sensing measurements of streambank migration and erodibility, *Earth Surf. Processes Landforms*, *27*(6), 627–639, doi:10.1002/esp.338.
Montgomery, K. (1993), Non-linear dynamics and river meandering, *Area*, *25*(2), 97–108.
Montgomery, K. (1996), Sinuosity and fractal dimension of meandering rivers, *Area*, *28*(4), 491–500.
Mosselman, E. (1998), Morphological modelling of rivers with erodible banks, *Hydrol. Processes*, *12.8*, 1357–1370.

Motta, D., J. D. Abad, E. J. Langendoen, and M. H. Garcia (2012a), The effects of floodplain soil heterogeneity on meander planform shape, *Water Resour. Res.*, *48*, W09518, doi:10.1029/2011WR011601.
Motta, D., J. D. Abad, E. J. Langendoen, and M. H. Garcia (2012b), A simplified 2D model for meander migration with physically-based bank evolution, *Geomorphology*, *163-164*, 10–25, doi:10.1016/j.geomorph.2011.06.036.
Nagata, T., Y. Watanabe, H. Yasuda, and A. Ito (2014), Development of a meandering channel caused by the planform shape of the river bank, *Earth Surf. Dyn.*, *2*(1), 255–270, doi:10.5194/esurf-2-255-2014.
Nanson, G. C., and E. J. Hickin (1983), Channel migration and incision on the Beatton River, *J. Hydraul. Eng.*, *109*(3), 327–337.
Odgaard, A. (1987), Streambank erosion along two rivers in Iowa, *Water Resour. Res.*, *23*(7), 1225–1236.
Orfanidis, S. J. (1996), *Introduction to Signal Processing*, Prentice-Hall, Englewood Cliffs, N. J.
Ori, G., F. Cannarsa, F. Salese, I. Dell'Arciprete, and G. Komatsu (2013), Why braided streams are apparently absent but there are meander and low-sinuosity single-channels river systems on Mars, *Proc. Lunar Planet. Sci. Conf. 44th,* pp. 3–4, The Woodlands, Tex., 18–22 March.
Parker, G., and E. D. Andrews (1986), On the time development of meander bends, *J. Fluid Mech.*, *162*, 139–156, doi:10.1017/S0022112086001970.
Parker, G., Y. Shimizu, G. V. Wilkerson, E. C. Eke, J. D. Abad, J. W. Lauer, C. Paola, W. E. Dietrich, and V. R. Voller (2011), A new framework for modeling the migration of meandering rivers, *Earth Surf. Processes Landforms*, *36*(1), 70–86, doi:10.1002/esp.2113.
Perucca, E., C. Camporeale, and L. Ridolfi (2005), Nonlinear analysis of the geometry of meandering rivers, *Geophys. Res. Lett.*, *32*, L03402, doi:10.1029/2004GL021966.
Perucca, E., C. Camporeale, and L. Ridolfi (2007), Significance of the riparian vegetation dynamics on meandering river morphodynamics, *Water Resour. Res.*, *43*, W03430, doi:10.1029/2006WR005234.
Pittaluga, M. B., and G. Seminara (2011), Nonlinearity and unsteadiness in river meandering: A review of progress in theory and modelling, *Earth Surf. Processes Landforms*, *36*(1), 20–38, doi:10.1002/esp.2089.
Pizzuto, J. E., and T. S. Meckelnburg (1989), Evaluation of a linear bank erosion equation, *Water Resour. Res.*, *25*(5), 1005–1013, doi:10.1029/WR025i005p01005.
Posner, A. J., and J. G. Duan (2012), Simulating river meandering processes using stochastic bank erosion coefficient, *Geomorphology*, *163-164*, 26–36, doi:10.1016/j.geomorph.2011.05.025.
Quraishy, M. (1944), The origin of curves in rivers, *Curr. Sci.*, *13*, 36–39.
Rossell, R. P., and F. C. K. Ting (2013), Hydraulic and contraction scour analysis of a meandering channel: James River Bridges near Mitchell, South Dakota, *J. Hydraul. Eng.*, *139*, 1286–1296, doi:10.1061/(ASCE)HY.1943-7900.0000791.
Rüther, N., and N. Olsen (2007), Modelling free-forming meander evolution in a laboratory channel using three-dimensional computational fluid dynamics, *Geomorphology*, *89*(3-4), 308–319, doi:10.1016/j.geomorph.2006.12.009.
Schumm, S. (1985), Patterns of alluvial rivers, *Annu. Rev. Earth Planet. Sci.*, *13*, 5–27.
Seminara, G. (2006), Meanders, *J. Fluid Mech.*, *554*, 271–297, doi:10.1017/S0022112006008925.
Seminara, G., and M. B. Pittaluga (2012), Reductionist versus holistic approaches to the study of river meandering: An ideal dialogue, *Geomorphology*, *163-164*, 110–117, doi:10.1016/j.geomorph.2011.06.037.
Seminara, G., G. Zolezzi, M. Tubino, and D. Zardi (2001), Downstream and upstream influence in river meandering. Part 2. Planimetric development, *J. Fluid Mech.*, *438*, 213–230, doi:10.1017/S0022112001004281.
Shields, F. D., Jr., S. S. Knight, and J. M. Stofleth (2005), Alternatives for riverine backwater restoration by manipulation of severed meander bend, in *Proceedings of the 2005 World Water and Environmental Resources Congress: Impacts of Global Climate Change*, edited by Walton, R., pp. 1–12, Am. Soc. of Civ. Eng., Reston, Va., doi:10.1061/40792(173)566.
Snow, R. S. (1989), Fractal sinuosity of stream channels, *Pure Appl. Geophys.*, *131*(1-2), 99–109, doi:10.1007/BF00874482.
Stolum, H.-H. (1996), River meandering as a self-organization process, *Science*, *271*, 1710–1713.
Stolum, H.-H. (1998), Planform geometry and dynamics of meandering rivers, *Geol. Soc. Am. Bull.*, *110*(11), 1485–1498, doi:10.1130/0016-7606(1998)110<1485:PGADOM>2.3.CO;2.
Struiksma, N., K. W. Olesen, C. Flokstra, and H. J. De Vriend (1985), Bed deformation in curved alluvial channels, *J. Hydraul. Res.*, *23*(1), 57–79, doi:10.1080/00221688509499377.
Sun, T., and P. Meakin (1996), A simulation model for meandering rivers, *Water Resour. Res.*, *32*(9), 2937–2954.
Sun, T., P. Meakin, and T. Jøssang (2001), A computer model for meandering rivers with multiple bed load sediment sizes: 2. Computer simulations, *Water Resour. Res.*, *37*(8), 2243–2258.
Swanson, D. (1993), The importance of fluvial processes and related reservoir deposits, *J. Pet. Technol.*, *45*(4), 368–377, doi:10.2118/23722-PA.
Utcke, S. (2003), Error-bounds on curvature estimation, in *Proceedings of Scale Space Methods in Computer Vision (SSMC'2003), volume 2695 of LNCS*, pp. 1080–1089, Springer, Berlin.
van de Lageweg, W. I., W. M. van Dijk, and M. G. Kleinhans (2013), Channel belt architecture formed by a meandering river, *Sedimentology*, *60*(3), 840–859, doi:10.1111/j.1365-3091.2012.01365.x.
Wallick, J. R., S. T. Lancaster, and J. P. Bolte (2006), Determination of bank erodibility for natural and anthropogenic bank materials using a model of lateral migration and observed erosion along the Willamette River, Oregon, USA, *River Res. Appl.*, *22*(6), 631–649, doi:10.1002/rra.925.
Weihaupt, J. (1974), Possible origin and probable discharges of meandering channels on the planet Mars, *J. Geophys. Res.*, *79*(14), 2073–2076.
Worring, M., and A. Smeulders (1993), Digital curvature estimation, *CVGIP: Image Understanding*, *58*(3), 366–382.
Xu, D., Y. Bai, J. Ma, and Y. Tan (2011), Numerical investigation of long-term planform dynamics and stability of river meandering on fluvial floodplains, *Geomorphology*, *132*(3-4), 195–207, doi:10.1016/j.geomorph.2011.05.009.
Yao, Z., J. Xiao, W. Ta, and X. Jia (2012), Planform channel dynamics along the Ningxia-Inner Mongolia reaches of the Yellow River from 1958 to 2008: Analysis using Landsat images and topographic maps, *Environ. Earth Sci.*, *70*(1), 97–106, doi:10.1007/s12665-012-2106-0.
Zolezzi, G., and G. Seminara (2001), Downstream and upstream influence in river meandering. Part 1. General theory and application to overdeepening, *J. Fluid Mech.*, *438*, 183–211, doi:10.1017/S0022112001004281.